AGU PUBLICATIONS

Journal of Advances in Modeling Earth Systems

RESEARCH ARTICLE

10.1002/2017MS000981

Understanding Mesoscale Aggregation of Shallow Cumulus Convection Using Large-Eddy Simulation

C. S. Bretherton[1] and P. N. Blossey[1]

[1]Department of Atmospheric Sciences, University of Washington, Seattle, WA, USA

Key Points:
- In large-domain LES of shallow cumulus convection, mesoscale moist patches containing clusters of vigorous cumuli develop within 1–2 days
- The moisture aggregation is analyzed with the weak temperature gradient approximation and mesoscale moisture budgets
- Gross moist instability drives aggregation even without precipitation and with horizontally uniform radiative and surface fluxes

Correspondence to:
C. Bretherton,
breth@washington.edu

Citation:
Bretherton, C. S., & Blossey, P. N. (2017). Understanding mesoscale aggregation of shallow cumulus convection using large-eddy simulation. *Journal of Advances in Modeling Earth Systems*, *9*, 2798–2821. https://doi.org/10.1002/2017MS000981

Received 21 MAR 2017
Accepted 17 OCT 2017
Accepted article online 20 OCT 2017
Published online 4 DEC 2017

Abstract Marine shallow cumulus convection, often mixed with thin stratocumulus, is commonly aggregated into mesoscale patches. The mechanism and conditions supporting this aggregation are elucidated using 36 h large-eddy simulations (LES) on a 128 × 128 km doubly periodic domain, using climatological summertime forcings for a location southeast of Hawaii. Within 12 h, mesoscale patches of higher humidity, more vigorous cumulus convection, and thin detrained cloud at the trade inversion base develop spontaneously. Mesoscale 16 × 16 km subdomains are composited into quartiles of column total water path and their heat and moisture budgets analyzed. The weak temperature gradient approximation is used to explain how apparent heating perturbations drive simulated mesoscale circulations, which in turn induce relative moistening of the moistest subdomains, a form of gross moist instability. Self-aggregation is affected by precipitation and mesoscale feedbacks of radiative and surface fluxes but still occurs without them. In that minimal-physics setting, the humidity budget analysis suggests self-aggregation is more likely if horizontal-mean humidity is a concave function of the horizontal-mean virtual potential temperature, a condition favored by radiative cooling and cold advection within the boundary layer.

Plain Language Summary Fair-weather cumulus clouds cover much of the low-latitude oceans. They are typically observed in clusters or lines spaced 50-100 km apart, often surrounded by thin patches of more extensive cloud. This clustering process is studied with a numerical model that covers a region large enough to encompass a typical cluster, using a grid fine enough to simulate the turbulent updrafts that create individual clouds. We find that clustering robustly occurs within one to three days, even in the absence of factors previously thought to be essential, such as precipitation. A simple conceptual model based on feedbacks between cumulus convection and humidity is developed to explain the clustering process, and it is validated against our simulations.

1. Introduction

Figure 1 shows a microwave retrieval of column water vapor path overlaid on a visible image centered at 17°N, 149°W, from the NASA A-Train satellite constellation on 14 July 2015. This location is toward the downstream edge of the climatological stratocumulus (Sc) to shallow cumulus (Cu) transition over the subtropical northeast Pacific Ocean. Figure 1 shows a typical example of the summertime cloud organization at this location, mesoscale clusters of Cu 2–3 km deep rising into surrounding patches of thin Sc. There is also mesoscale variability in the column water vapor path, and the cumulus clusters tend to lie within moist patches. We refer to this as an "aggregated" state of humidity and cumulus convection, since one could imagine a much more homogeneous distribution of these quantities on the mesoscale. This paper aims to develop an improved understanding of how feedbacks between humidity, shallow cumulus convection and related processes may promote this aggregation.

Marine boundary layer cloud regimes worldwide exhibit mesoscale organization, often in the form of the regular patterns of mesoscale cellular convection or MCC (Agee et al., 1973) with a roughly 30:1 aspect ratio of the wavelength to the boundary layer depth (Agee et al., 1973; Wood & Hartmann, 2006). These include closed cells in shallow stratocumulus layers, and open cells in cumulus and mixed Cu-Sc layers, in both extratropical cold-air outbreaks and subtropical boundary layers. Cumulus clusters like those in Figure 1a have been interpreted as "disorganized" MCC, which satellite imagery suggests becomes a prevalent form of cloud organization as the marine boundary layer deepens to 2 km or more (Wood & Hartmann, 2006).

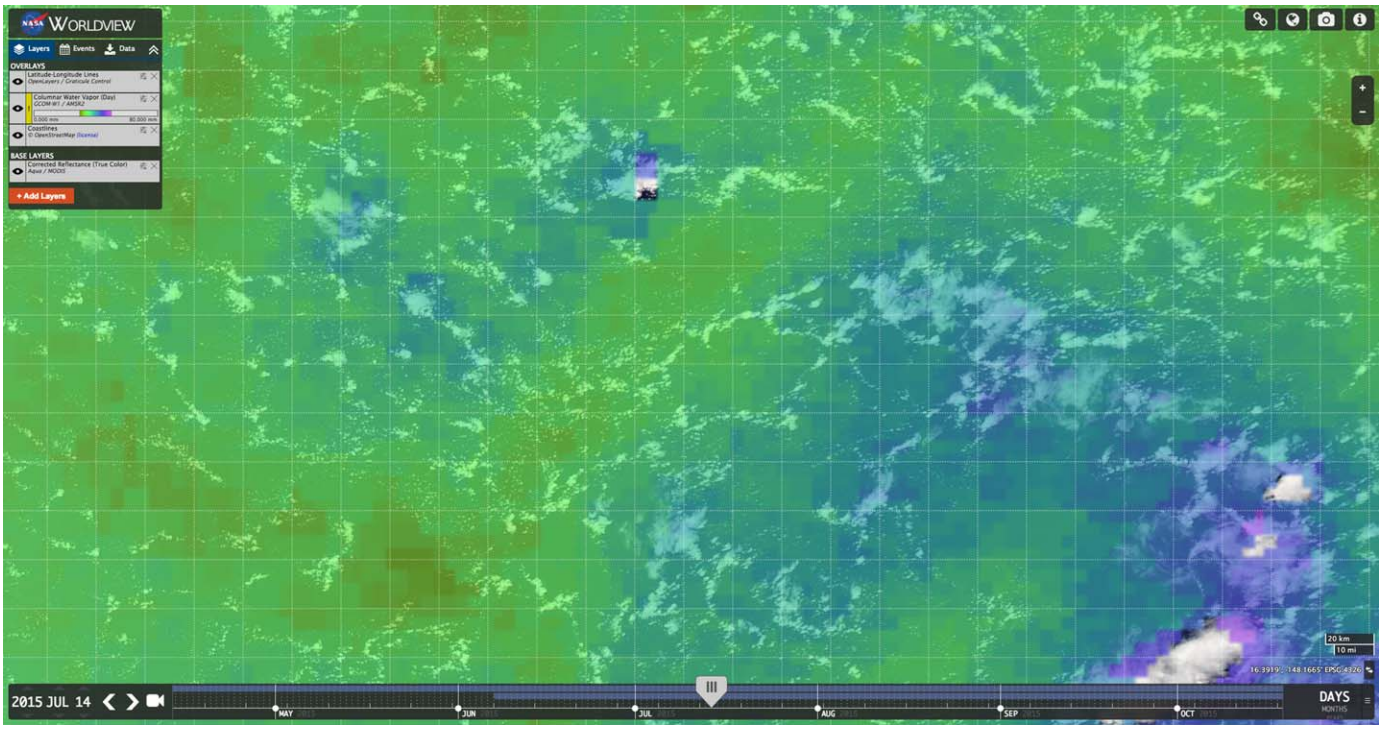

Figure 1. AMSR-2 microwave retrieval of column water vapor path (shading, ranging from 30 kg/m^2 in brownish-green to 45 kg/m^2 in purple) overlaid on a visible image from Aqua over a region of aggregated shallow cumulus centered at 17°N, 149°W at about 13:30 local time on 14 July 2015. The overlaid latitude-longitude grid has a spacing of 0.2°. Image is generated from NASA Worldview (https://worldview.earthdata.nasa.gov).

Pioneering early observational studies of shallow cumuli over the tropical oceans already noted its propensity to cluster on the mesoscale (LeMone & Meitin, 1984; Malkus & Riehl, 1964).

Numerous theoretical and modeling studies have tried to explain the large aspect ratio of the wavelength of MCC to the boundary layer depth. Early studies interpreted MCC as a form of Rayleigh-Benard convection (Agee et al., 1973). MCC has a much larger aspect ratio than the 5:1 aspect ratio of dry surface-forced thermal convection (Schroeter et al., 2005); this was rationalized using mechanisms such as anisotropic eddy viscosity or constant-flux boundary conditions (Agee et al., 1973). However, these mechanisms do not explain the multiscale turbulent character of MCC seen in observations and LES; most of the vertical velocity variance remains in eddy motions of aspect ratios of 3–5 despite the large aspect ratio of clouds and water vapor (Rothermel & Agee, 1980; Schroeter et al., 2005). This motivated two new theories of MCC. The first, mesoscale entrainment instability (Fiedler, 1984), only applies to very unusual thermal inversion structures, so it cannot explain the ubiquity of MCC. The second is that MCC forms from entrainment-related production of mesoscale humidity variance, e.g., De Roode et al. (2004), which can occur even in a dry-convective boundary layer (Jonker et al., 1999) but is promoted by latent heating and cloud top radiative cooling (Mueller & Chlond, 1996). This mechanism was applied to closed-cell convection and idealizations thereof, for which LES suggests a gradual increase in aspect ratio as humidity variance grows at large scales. De Roode et al. (2004) proposed that a humidity variance budget equation could be a useful diagnostic for understanding MCC. Kazil et al. (2017) suggested that inefficient production of turbulent kinetic energy at longer wavelengths limits the width of closed cells; however, they focused on the subtle influence of cell scale on the horizontal-mean properties of a simulated stratocumulus-capped mixed layer rather than on a systematic analysis of how horizontal humidity variance is generated.

LES have shown that precipitation influences MCC. It can force transitions from closed to open cell MCC by enhancing decoupling and cold pool organization (Wang & Feingold, 2009), reinforced by aerosol feedbacks, as in pockets of open cells (Berner et al., 2013). Seifert and Heus (2013) presented LES of mesoscale organization of precipitating shallow cumulus boundary layers. They found that the formation of cold pools by evaporating precipitation was a prerequisite for aggregation in their simulations, for the small

organizational scales achievable in $(25\ km)^2$ domains. A follow-on paper by Seifert et al. (2015) found that cold-pool driven mesoscale organization makes this cloud regime less susceptible to aerosol perturbations.

Other methodologies were developed to analyze the self-aggregation of deep cumulus convection first seen in cloud-resolving models (Bretherton et al., 2005; Held et al., 1993; Tompkins, 2001). These studies used column-integrated humidity budgets to isolate processes that further moisten mesoscale regions that are already moist. They noted the accuracy of the "weak temperature gradient" (WTG) approximation that mesoscale horizontal variations in air density (virtual temperature) are negligibly small for unbalanced circulations smaller than a Rossby radius (Bretherton et al., 2005; Sobel & Bretherton, 2000). This approximation has recently been exploited in combination with vertically resolved humidity and moist static energy budgets in analyses of the Madden-Julian Oscillation to associate vertical motions and their effects on the moisture budget with individual physical processes such as convection and radiative heating (Chikira, 2014; Wolding & Maloney, 2015).

We will use an analogous approach to understand mesoscale self-aggregation processes in LES of shallow cumulus. We frame self-aggregation as an instability of a horizontally statistically homogeneous field of cumulus clouds to the spontaneous growth of mesoscale humidity anomalies that span the cumulus layer, pattern the convection and clouds, and create heating perturbations that drive mesoscale circulations. We find that shallow cumulus can aggregate within a day or less due to a fundamentally advective aggregation mechanism different from the radiative feedbacks that are critical to deep-convective self-aggregation (e.g., Emanuel et al., 2014), and for which precipitation is not essential. This mechanism can be regarded as a form of gross moist instability (Raymond et al., 2009). In the simplest case, our mechanism seems related to that proposed for well-mixed stratocumulus by De Roode et al. (2004), and our use of mesoscale column humidity budgets is analogous to their use of a column-integrated humidity variance budget.

Section 2 introduces the LES configuration and key thermodynamic variables used in this analysis. Section 3 discusses the rate of self-aggregation in a control run and several sensitivity cases. Section 4 analyzes aggregation in the control simulation in terms of a unifying conceptual model based on the WTG approximation. Section 5 derives column mesoscale heat and moisture budgets that elucidate the conditions for self-aggregation, i.e., under which moist regions become moister and dry regions become drier. Section 6 considers the mesoscale self-aggregation of shallow cumulus in a minimal-physics setup without precipitation and with horizontally homogeneous radiative heating and surface fluxes. Section 7 presents a discussion and conclusions.

2. Thermodynamic Variables and LES Model Configuration

2.1. SAM LES Model

The LES model used in this study is version 6.10 of the System for Atmospheric Modeling (SAM), kindly supplied and maintained by Marat Khairoutdinov and documented by Khairoutdinov and Randall (2003) and Blossey et al. (2013). All of our simulations are restricted to warm clouds with liquid condensate only, so the remaining discussion assumes liquid cloud thermodynamics and microphysics. For this case, SAM prognoses four advected scalars, the liquid static energy s_l, the nonprecipitating water mixing ratio $q_n = q_v + q_c$, the rain water mixing ratio q_r, and rain number concentration N_r. The cloud liquid water and temperature are diagnosed from the advected scalars using the assumption of exact grid-scale saturation in cloudy grid cells. Here q_v and q_c are the mixing ratios of water vapor and cloud water, and the liquid static energy is defined

$$s_l = s - L_v(q_c + q_r), \tag{1}$$

where static energy $s = c_p T + gz$, c_p is the isobaric specific heat of dry air, L_v is the latent heat of vaporization, g is gravity, T is temperature, and z is height above sea level.

The warm cloud version of the Morrison et al. (2005) microphysics scheme is used in these simulations. In this scheme, conversion between cloud and rain water is treated according to Khairoutdinov and Kogan (2000). The cloud droplet size distribution is based on a gamma distribution with a fixed number concentration of $N_d = 100\ cm^{-3}$ and an exponent $\mu = 10.3$ (Geoffroy et al., 2010). This cloud droplet size distribution is used to compute cloud droplet sedimentation and the optical properties of cloud liquid (Neale et al.,

2012, section 4.9.3). Radiative fluxes are updated every 60 s using the RRTMG scheme (Mlawer et al., 1997), with diurnally averaged insolation following Blossey et al. (2013).

2.2. Domain Size and Grid Resolution

A doubly periodic domain of horizontal size 128 × 128 km is used. We choose a relatively coarse grid for computational efficiency, with a horizontal grid spacing of 250 m and a vertical grid spacing that is uniformly 80 m up to 6 km with a stretched grid above, extending to the domain top at 20 km. The computational domain has 512 × 512 × 128 grid points in x, y, and z, respectively. All simulations are run for 36 h unless otherwise noted, with an adaptive time step whose average value is 2.5 s.

2.3. Control Simulation

The control simulation is based on summertime-mean thermodynamic profiles, advective forcings for 17°N, 149°W, the location shown in Figure 1, which is typified by exactly the mesoscale clusters of Cu rising into surrounding patches of thin Sc that we aim to simulate and understand. It mainly follows the S6 specifications for the CGILS intercomparison (Blossey et al., 2013) but differs in the following details:

1. The duration of the simulation is 72 h, rather than 10 days.
2. Rotational effects are included, using the Coriolis parameter for 17°N. The geostrophic winds are taken equal to the ECMWF winds. The simulated domain-mean wind profile is also nudged to the ECMWF wind profile on a long, 12 h time scale. The standard CGILS setup nudged the model winds on a 10 minute time scale. To minimize oscillations of the winds, the initial wind profiles are the average wind profile over the last 6 days of a 13.5 day small-domain ($L_x = L_y = 8$ km) simulation.
3. The surface fluxes are computed interactively using SAM's surface flux parameterizations and account for local variations in surface wind speed, unlike the idealized surface flux parameterization used in Blossey et al. (2013).
4. The domain is uniformly translated by the approximate mean wind in the cloud layer ($u = -8.5$ m s^{-1} and $v = -3$ m s^{-1}), rather than -7 and -2 m s^{-1}, respectively, in Blossey et al. (2013). This minimizes the advection of aggregated patches of cumulus convection across the domain.

2.4. Prognostic Equations for s_l and q_t

In our LES, the prognostic equation for s_l is

$$\frac{Ds_l}{Dt} = S_{sl} = -\frac{1}{\rho_0}\frac{\partial}{\partial z}(L_v P + F_R) + \left(\frac{\partial \overline{s}_l}{\partial t}\right)_{LS} - w_{LS}\frac{\partial s_l'}{\partial z} + \left(\frac{\partial s_l}{\partial t}\right)_{SGS}, \tag{2}$$

where D/Dt denotes a material derivative, S denotes a source term, $\rho_0(z)$ is the fixed reference density profile, P is the downward precipitation flux relative to the moving air, F_R is the net upward radiative flux, subscript LS refers to large-scale advective forcing (here split into a horizontally uniform component regarded as being applied to the horizontal mean, and vertical advection by w_{LS} of perturbations s_l' from the horizontal mean), and subgrid SGS refers to parameterized subgrid turbulence.

A similar prognostic equation is solved in SAM for q_n. However, for budget purposes, it is more elegant to frame the prognostic equation for water substance in terms of the total water mixing ratio $q_t = q_v + q_c + q_r = q_n + q_r$:

$$\frac{Dq_t}{Dt} = S_{qt} = \frac{1}{\rho_0}\frac{\partial P}{\partial z} + \left(\frac{\partial \overline{q}_t}{\partial t}\right)_{LS} - w_{LS}\frac{\partial q_t'}{\partial z} + \left(\frac{\partial q_t}{\partial t}\right)_{SGS}. \tag{3}$$

The mass-weighted vertical integral of q_t, which is the sum of the water vapor path and the liquid water path (LWP), will be called the total water path (TWP).

2.5. Prognostic Equation for s_{vl}

Horizontal gradients of air density or buoyancy are central to the dynamics of moist convective boundary layers. We use virtual static energy,

$$s_v = c_p T_v + gz, \tag{4}$$

as a buoyancy proxy. Here the virtual temperature $T_v = T(1 + 0.61 q_v - q_c - q_r)$ is assumed to include the loading effect of cloud water and rain water mixing ratio q_r. We stress that while we must consider virtual effects

on air density in our quantitative analysis because our LES (correctly) includes them, we do not believe that they fundamentally affect the mechanisms discussed in this paper. That is, if our model neglected these virtual effects, it would have little impact on the simulated aggregation.

For analysis of transport, fluxes, and budgets, it is helpful to work with moist-conserved variables. The linearized virtual liquid static energy,

$$s_{vl} = s_l + 0.61 c_p T_0 q_t, \tag{5}$$

where T_0 is a reference temperature representative of the boundary layer, is a moist-conserved variable that is an excellent approximation to s_v for unsaturated air, since

$$s_v \approx s_{vl} + (L_v - 1.61 c_p T_0)(q_c + q_r). \tag{6}$$

In this paper, "heat" budgets will actually refer to budgets of s_{vl}. The prognostic equation for s_{vl}, derived from (3) and (2), is

$$\frac{Ds_{vl}}{Dt} = S_{svl} = -\frac{1}{\rho_0}\frac{\partial}{\partial z}\left((L_v - 0.61 c_p T_0)P + F_R\right) + \left(\frac{\partial \bar{s}_{vl}}{\partial t}\right)_{LS} - w_{LS}\frac{\partial s'_{vl}}{\partial z} + \left(\frac{\partial s_{vl}}{\partial t}\right)_{SGS}. \tag{7}$$

3. Mean Evolution and Aggregation of the Control and Sensitivity Simulations

3.1. Domain-Mean Evolution

Figure 2 shows the time-height evolution of the horizontal means of several key variables in the first 36 h of the control simulation and in two 36 h simulations in much smaller domains (8 km^2) that do not support the development of mesoscale variability. One (S250) is identical to the control run except in domain size; the second (S125) also has a grid spacing half as large (125 m in the horizontal and 40 m in the vertical within the boundary layer).

All of these simulations have a similar horizontal-mean cloud evolution (Figures 2a–2c), with a cumulus-topped boundary layer developing after 2 h, deepening rapidly and developing patchy inversion cloud after 6–7 h and reaching a depth of 2 km by the end of the simulation. The control and S250 simulations also have very similar time series of LWP and shortwave cloud radiative effect (SWCRE). De Roode et al. (2004) and Xue et al. (2008) noted a similar insensitivity of horizontal-mean properties of shallow boundary layer cloud layers to use of a domain size large enough to permit substantial mesoscale organization.

In the control simulation, precipitation sets in after 12 h and reaches a domain-mean precipitation rate of over 1 mm/d by 36 h. The precipitation is substantially delayed in the small-domain simulations (as also

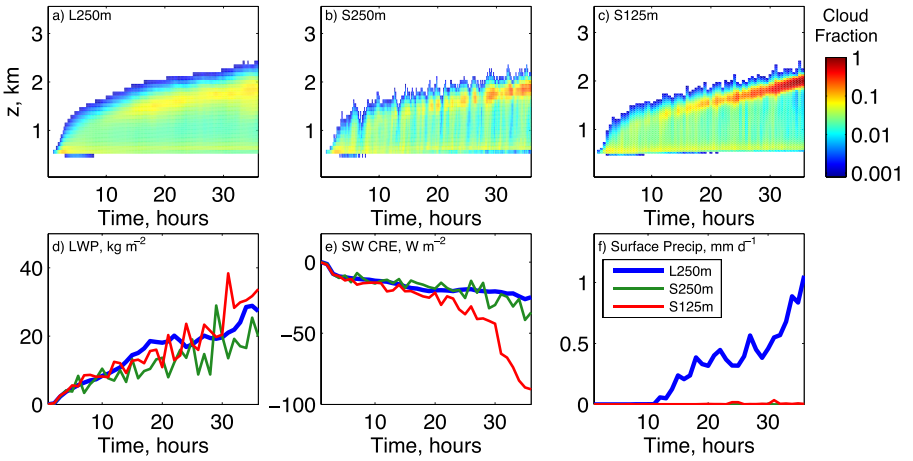

Figure 2. Time-height profiles of horizontally averaged cloud fraction for (a) the control simulation (L250) with horizontal grid spacing $\Delta x = 250$ m), and two other simulations, (b) S250m and (c) S125m, that are identically configured except for domain size, $L_x = L_y = 8$ km, and—in the case of S125m, the horizontal grid spacing $\Delta x = 125$ m. At bottom, time series of domain-mean (d) liquid water path, (e) shortwave cloud radiative effect, and (f) surface precipitation.

noted by Vogel et al., 2016); continuations of these simulations do later generate substantial domain-precipitation rates. Though this disparity in precipitation has little effect on the cloud properties during our simulations, that would likely change if the boundary layer deepens further. Vogel et al. (2016) found domain-size sensitivities in domain-mean cloud cover for a precipitating cumulus layer once some cloud tops in the large-domain simulation exceeded 4 km altitude.

Figure 2 shows that for our case, the domain-mean cloud fraction is more sensitive to doubling of grid resolution than changes in domain size. Enhanced grid resolution increases the cloud fraction near the inversion, an indicator of reduced penetrative entrainment at stratocumulus and cumulus cloud tops. This substantially increases the SWCRE toward the end of the simulations.

Despite these quantitative sensitivities, our sensitivity experiments do not show a qualitative change in the cloud and boundary layer structure for a finer grid. A more compelling reason to use a finer grid comes from simulations of deep-convective radiative-convective equilibrium, in which aggregation occurs more readily with a coarser grid (Muller & Held, 2012). Large-domain simulations with finer grids were too computationally expensive for this study. Our hope is that an analysis of aggregation in our large-domain control simulation is at least qualitatively relevant to simulations with similar or larger domain sizes and finer grid resolutions; that needs to be tested in future.

3.2. Horizontal Structure of the Aggregating Convection

The control simulation strongly aggregates within the first day of evolution. Figure 3 shows maps of TWP, LWP, and cloud top height at 8–32 h. During the first 8 h, a nearly horizontally homogeneous field of shallow cumulus develops as the underlying boundary layer becomes unstable and starts to convect. By hour 16, there are a few slightly moister (higher TWP) patches supporting clusters of deeper cumuli, surrounded by detrained cloud just below the inversion. These continue to amplify rapidly up through hour 24 and gradually combine into broader patches of moisture and collocated convection up until 32 h, when there is one main cluster in the domain. Little further qualitative change in the aggregation is seen out to the end of the simulation at 72 h.

Figure 4 shows a perspective plot of the simulated cloud field after 32 h, periodically translated 48 km in the *x* direction to avoid visually splitting the main cluster at one of the periodic boundaries of the

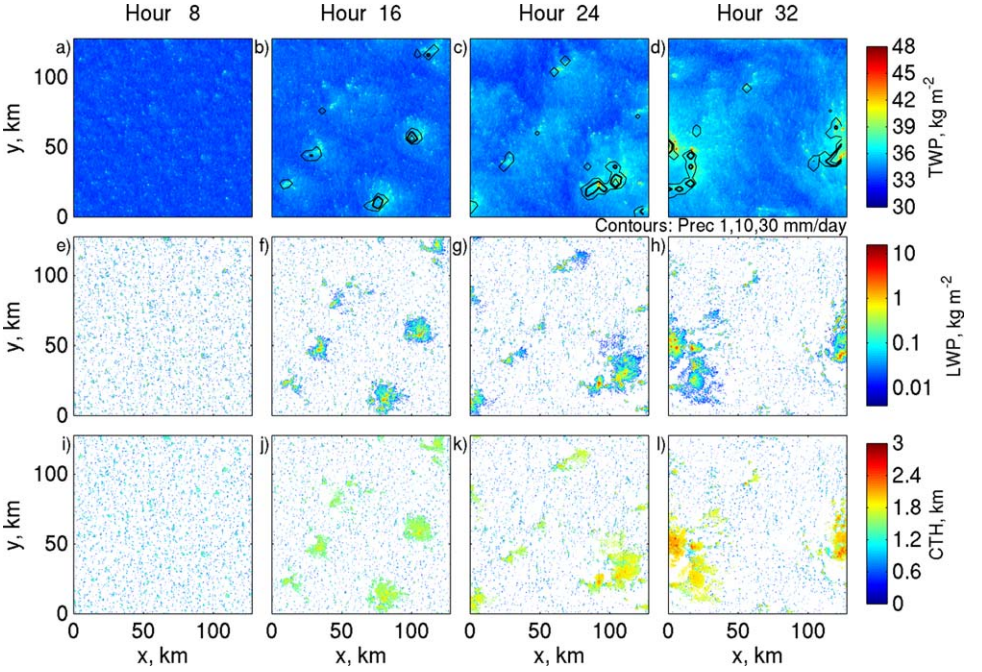

Figure 3. (a–d) Total water path, (e–h) liquid water path, and (i–l) cloud top height in the control simulation at (Figures 3a, 3e, and 3i) 8 h, (Figures 3b, 3f, and 3j) 16 h, (Figures 3c, 3g, and 3k) 24 h, and (Figures 3d, 3h, and 3l) 32 h.

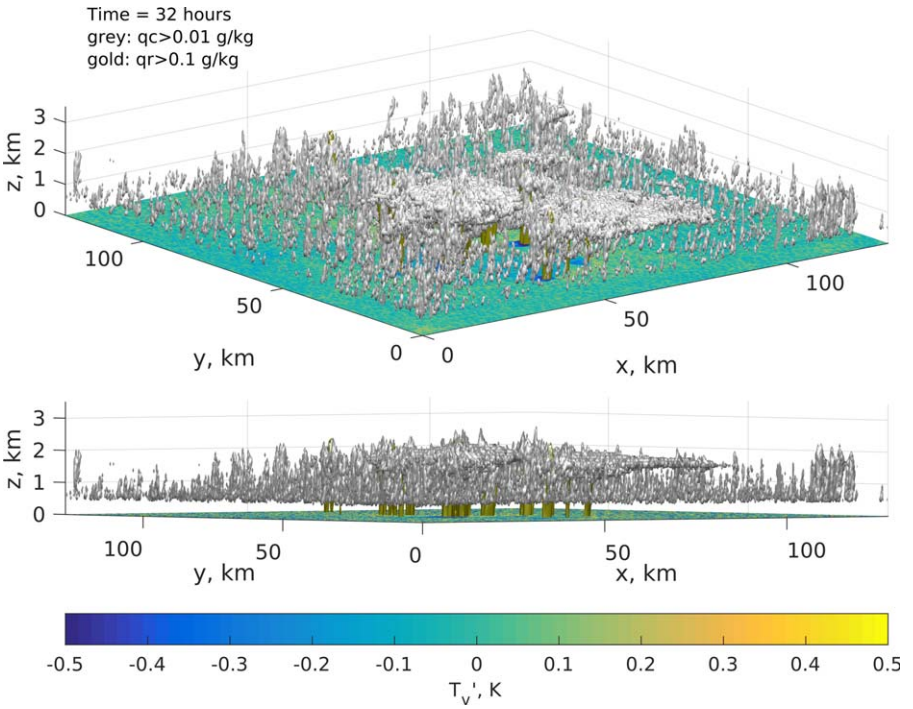

Figure 4. Perspective plot of the cloud field ($q_c > 0.01$ g/kg) and rain ($q_r > 0.1$ g/kg, gold shading) at 32 h in the control simulation. Sea-surface color shading indicates the virtual temperature anomaly at the lowest grid level. The displayed domain is periodically translated 48 km from the computational domain to avoid visually splitting the region of most active convection.

computational domain. Shallow cumuli surround the single mesoscale cluster of deeper precipitating cumuli and thin inversion cloud.

3.3. Block and Quartile Description of Aggregation

To quantify the evolution of mesoscale variability in the simulated cloud-topped boundary layer, we use means and other statistics over $(16\ \text{km})^2$ horizontal blocks of grid points, averaged over 2 h periods. These mesoscale blocks have been chosen to be large enough to contain an ensemble of clouds sufficient that the block-mean vertical Cu fluxes are a well-defined function of the block-mean thermodynamic profiles (and radiation and surface fluxes, if also needed), but small enough that the simulated aggregation scale is larger than the block size. From Figures 3a–3d, growing column humidity anomalies have diameters on the order of 20 km at 16 h, and broaden at later times; these scales are efficiently captured with our chosen block size. A similar procedure for analyzing deep-convective self-aggregation was introduced by Bretherton et al. (2005). Other large-scale/small-scale decompositions which additively partition variance could also be used, e.g., Fourier low/high pass filtering or some form of wavelet decomposition. The block decomposition has the substantial advantage that all the needed fields and statistics can easily be averaged and saved in-line at each time step within each block, allowing them to be time averaged and efficiently stored. We denote perturbations of a mesoscale block average of some quantity from its domain mean using a subscript m.

Following Bretherton et al. (2005), we sort the 64 mesoscale blocks in our computational domain in increasing order of total water path. To summarize the mesoscale variations that are associated with differences between moist and dry blocks, we compute quartile averages over these blocks, with Q1 being the driest quartile and Q4 being the moistest quartile. For plotting clarity, we will sometimes lump the two intermediate quartiles Q2 and Q3 together. The quartile averaging is always with respect to TWP, regardless of the plotted variable. Note that the quartile plots do not show the length scale of the variability, as long as it is large enough to be resolved by the 16 km block size.

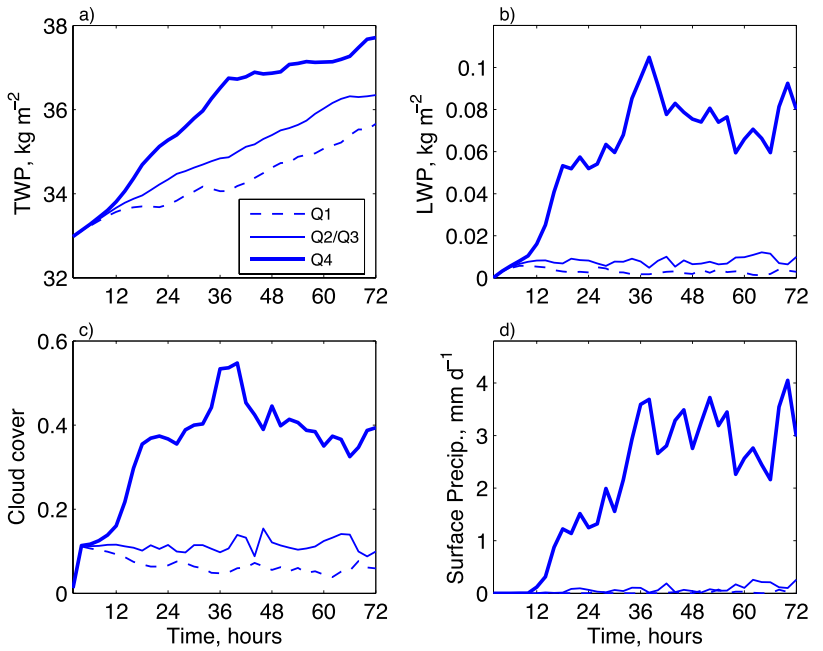

Figure 5. Column humidity quartile-sorted time series of (a) total water path, (b) liquid water path, (c) cloud cover, and (d) surface precipitation in the control simulation.

Figure 5 shows such moisture quartile plots for TWP, LWP, cloud cover (the fraction of columns in the domain containing any cloud), and rainfall. These plots summarize the aggregation process. At 8 h, there is very little TWP variability on scales larger than the width of a single cumulus cloud (Figure 3a). Figure 5a shows that the TWP of the moistest and driest quartiles begin to diverge soon thereafter. Their difference grows nearly exponentially through hour 16, continues to rapidly grow through hour 24, grows more slowly until hour 36, then levels off and even slightly reduces. This growth of the "interquartile" Q4–Q1 TWP difference is the defining characteristic of mesoscale humidity aggregation. After aggregation develops, the LWP, cloud cover and rainfall are strongly localized to the moistest quartile, consistent with the visual impression from Figures 3c and 3d.

While the humidity and cloud aggregation may be regarded as an instability of a state of horizontally homogeneous shallow cumulus convection, it quickly deviates from the expectations of linear instability theory. For an exponentially growing linear instability, one would expect the Q4 and Q1 results to diverge exponentially with time, with the Q2/Q3 average lying half way in between them. In LWP, cloud fraction and precipitation, such behavior is limited to hours 8–11, after which nonlinearities become obvious. The BOMEX sensitivity study in section 3.4, in which no extensive cloud patches form at the inversion, does exhibit a much longer period of slow exponential growth in the TWP quartile separation, suggesting that inversion cloud patches that form only in the moistest quartile may be one such source of nonlinearity.

3.4. Sensitivity Simulations

We performed several sensitivity simulations, summarized in Table 1 (which also includes the two small-domain simulations discussed in section 3.1) to look for factors controlling the existence and rate of aggregation. Figures 6a–6c show quartile plots of TWP and LWP for these simulations, except Diurnal and FixedInv. All sensitivity simulations last 36 h, except BOMEX, which spans 72 h.

Simulations Diurnal and FixedInv test the robustness of features of our case setup. For brevity, these simulations are described without supporting figures. Simulation Diurnal includes a diurnal cycle of insolation corresponding to the S6 location, assuming the simulation is initialized at 0 UTC, which is the late afternoon in local time. It aggregates quite similarly (in terms of Q4–Q1 TWP spread) to CTL, as does a similar simulation initialized at 12 UTC.

Table 1
List of Sensitivity Simulations

Name	Description
Control	Based on present-day S6 case in Blossey et al. (2013), 128 × 128 km domain, Δx=250 m, Δz=80 m
S250	As in control, except with a small horizontal domain of 8 × 8 km
S125	As in S250, except using halved grid spacings Δx=125 m, Δz=40 m
Diurnal	As in control, but with diurnal cycle of insolation
FixedInv	As in control, but with mean subsidence increased to keep inversion height fixed
noPCP	As in control, except that rain formation and sedimentation are prohibited
RADhomo	As in control, except that radiative heating rates are horizontally homogenized
RFhomNoPCP	As in noPCP, except that both surface fluxes and radiative heating rates are horizontally homogenized
BOMEX	Based on BOMEX case in Siebesma et al. (2003), with same domain and grid as control

In FixedInv, the subsidence rate is adaptively adjusted to maintain a constant inversion height of 1,800 m using the method of Blossey et al. (2009). Again, the aggregation develops similarly to the control simulation, as measured by Q4–Q1 TWP spread, though the domain-mean TWP now stays nearly constant throughout the simulation. In FixedInv, the size of the moist patches does not grow as fast as in CTL, and stays smaller than the domain size throughout the simulation.

The remaining simulations test the sensitivity of the aggregation to changes in the physics included in the model, as well as the thermodynamic profiles assumed. Simulation noPCP is similar to the control (CTL), except that precipitation is suppressed. Figures 6a and 6c show that this has a minimal impact on the initial humidity and LWP aggregation, though it slightly reduces the aggregation at later times.

Simulation RADhomo is similar to CTL, except that the computed radiative heating rate is horizontally homogenized to prevent any local feedback on the growth of mesoscale cloud and humidity anomalies. Figures 6a and 6c show that the moisture and LWP begin to aggregate more slowly but later appear to catch up with, or in the case of LWP, exceed the aggregation evinced by CTL.

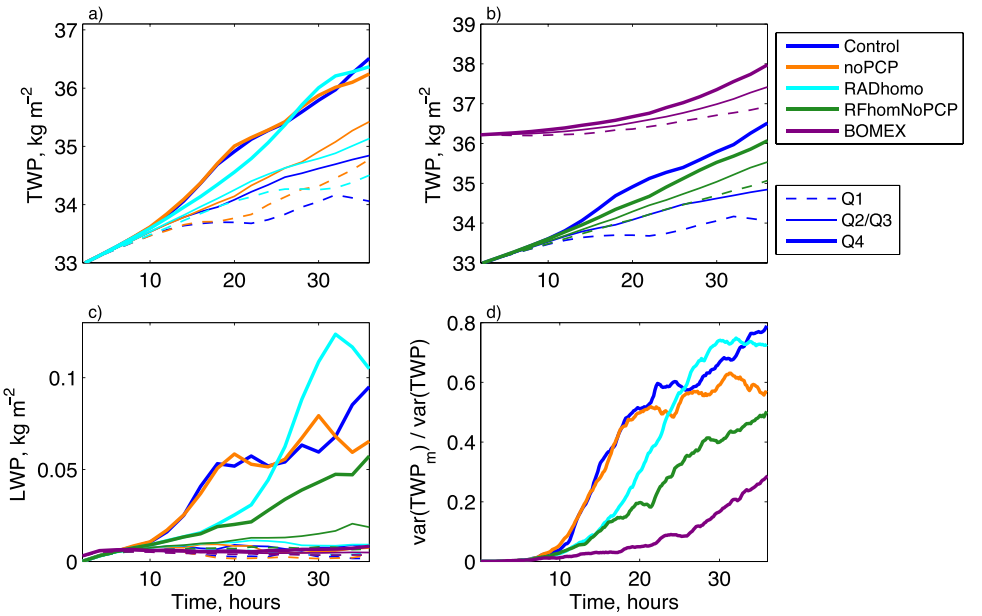

Figure 6. (top) Comparison of column humidity quartile-sorted time series of total water path for (a) control, no-precipitation (noPCP) and horizontally homogenized radiation (RADhomo) simulations and (b) control, nonprecipitating horizontally homogenized radiation and surface flux (RFhomNoPCP) and BOMEX simulations. Bottom: Comparisons for all sensitivity simulations of (c) column humidity quartile-sorted time series of liquid water path and (d) the ratio of the variance of the block-averaged total water path to that of the unfiltered total water path.

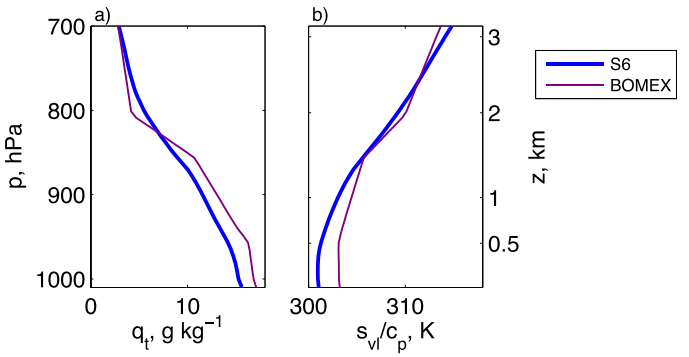

Figure 7. Initial profiles of (a) total water mixing ratio q_t and (b) virtual liquid static energy s_{vl}/c_p (a buoyancy surrogate outside cloud scaled into temperature units) for S6 and BOMEX.

In simulation RFhomNoPCP, both the radiative and surface fluxes are horizontally homogenized, and precipitation is suppressed. Our last sensitivity study uses a different initial thermodynamic profile and specified horizontally homogeneous advective/radiative and surface flux forcings from the GEWEX Cloud System Study Barbados Oceanographic and Meteorological Experiment (BOMEX) intercomparison (Siebesma et al., 2003). This simulation is also specified to be nonprecipitating. It is like RFhomNoPCP except that the initial temperature profile is less strongly stratified and the free troposphere is drier, as shown in Figure 7. Fixed forcing profiles for temperature and humidity tendency represent the combined effects of horizontal advection and radiative cooling.

Figure 6b compares moisture quartile time series from RFhomNoPCP and BOMEX with the control case. Both systematically aggregate column humidity, albeit more slowly than in CTL. We have continued the BOMEX simulation out to 72 h to confirm that the aggregation continues to develop. In the RFhomNoPCP case, inversion cloud patches that enhance LWP develop in the moistest quartile (Figure 6c). The BOMEX case does not sustain a large enough relative humidity at the inversion base to support inversion cloud. We speculate that this is due to its drier free troposphere and weaker lower tropospheric stability. As a result, BOMEX develops little LWP even in the moistest quartile, though still more than in the drier quartiles. In the BOMEX case, an approximately exponential growth of Q4–Q1 TWP difference with an *e*-folding time scale of about 15 h occurs throughout the simulation.

An alternate nondimensional metric of mesoscale aggregation can be formed by first calculating for each block its block-average ("mesoscale") total water path anomaly TWP_m from the domain mean. The ratio of the spatial variance of TWP_m to that of the raw TWP can be interpreted as the mesoscale fraction of the TWP variance. Figure 6d shows time series of this ratio for the simulations discussed thus far. It confirms that during the spread of Q4–Q1 TWP difference after hour 10 seen in Figures 6a and 6b, mesoscale variability starts to dominate the overall TWP variance between grid columns, indicating a state of mesoscale column humidity aggregation.

The TWP variance ratio metric can easily be quantitatively compared across cases and cloud regimes. Its dependence on the choice of block size should be weak for block sizes intermediate between the cumulus scale and the dominant aggregation scales. Alternate versions of the metric could be defined using other (possibly observationally derived) quantities, such as outgoing longwave radiation, as a complement to the cluster-based analysis of Tobin et al. (2012).

These sensitivity simulations suggest that neither precipitation nor mesoscale feedbacks of radiation or surface fluxes are essential for aggregation of a shallow cumulus boundary layer. However, local cloud-radiation feedback does speed up the initial moisture aggregation, and precipitation enhances aggregation toward the end of the simulation, as the boundary layer deepens and rains more.

4. Analysis of Aggregation of the Control Simulation

4.1. Moisture and Liquid Water Profiles

Figures 8a–8d show moisture quartile-sorted profiles of the mesoscale block-averaged humidity anomaly q_{tm} from the domain mean, averaged over 2 h blocks ending at 8, 16, 24, and 32 h. In the moistest quartile (Q4), the entire cumulus layer, from cloud base at 500 m to the highest cloud tops, is moistened, most strongly at the inversion base. By 24 h, the humidity anomaly at the inversion base reaches 1 g/kg, or about 10% in relative humidity, after which it grows much more slowly. Even as early as 16 h, the Q4 moisture anomalies are stronger and have a more top-heavy vertical profile than the dry quartile (Q1) anomalies. Remarkably, there are almost no mesoscale humidity perturbations in the subcloud layer, below 500 m altitude. This is because the sea surface temperature and the initial humidity field are horizontally homogeneous, and precipitation is too weak to drive vigorous cold pools that couple the subcloud layer temperature and humidity to the cumulus convection.

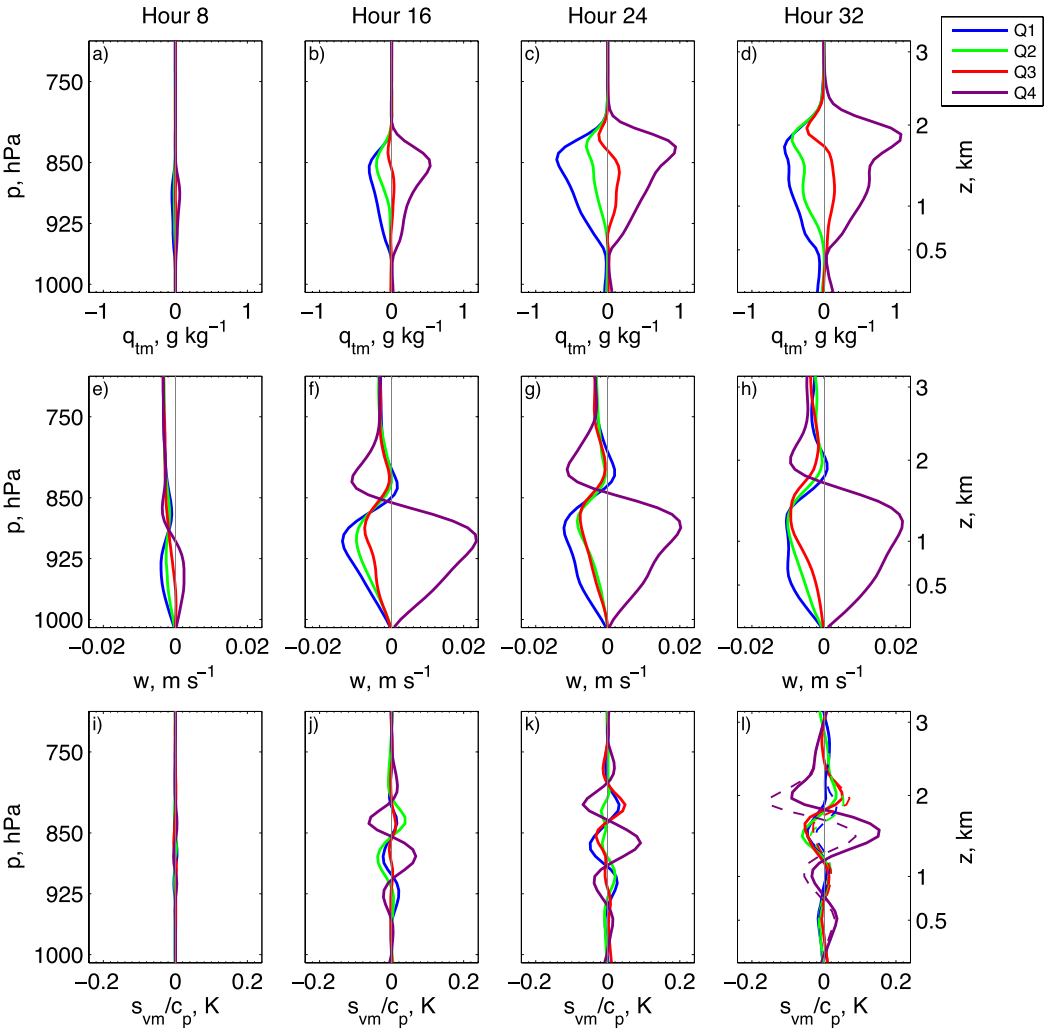

Figure 8. Column humidity quartile-sorted profiles of mesoscale anomalies (a–d) q_{tm}, (e–h) $w=\overline{w}+w_m$, and (i–l) s_{vm}/c_p averaged over 2 h periods ending at (Figures 8a, 8e, and 8i) 8 h, (Figures 8b, 8f, and 8j) 16 h, (Figures 8c, 8g, and 8k) 24 h, and (Figures 8d, 8h, and 8l) 32 h into the control simulation. For the final period, the mesoscale anomalies of virtual liquid static energy s_{vlm}/c_p are plotted as dashed lines along with those of s_{vm}/c_p in Figure 8l.

Figure 9 shows corresponding profiles of cloud fraction and cloud liquid water content q_c. They also show little interquartile separation near the cumulus base, but there is much more cloud in the moistest quartile throughout the rest of the cumulus layer and especially just below the inversion base. Remote sensing observations of Barbados trade cumuli by Nuijens et al. (2014) also show that cloud fraction is much more variable near the inversion than at the base of the cumulus layer on time scales of hours or longer.

Tropical shallow cumulus boundary layers do often show mesoscale moisture perturbations in the subcloud layer, which are correlated with overlying patches of shallow cumulus convection in observations (LeMone & Meitin, 1984) and in LES (Seifert & Heus, 2013). This patchiness may be a remnant of cold pools generated from prior precipitating convection, which take many hours to be damped out by surface flux feedbacks (Johnson & Nicholls, 1983). Subsynoptic humidity variability due to large-scale dynamics or mesoscale SST anomalies could also drive mesoscale humidity perturbations. Were such pre-existing perturbations added to the initial humidity distribution, they would likely modulate the early development of cumulus clouds and couple to the humidity-convection aggregation.

4.2. WTG Approximation

The bulk of a shallow cumulus boundary layer is stably stratified. Within and below active cumuli, condensation and evaporation can generate small-scale heating and buoyancy anomalies. Gravity waves constantly

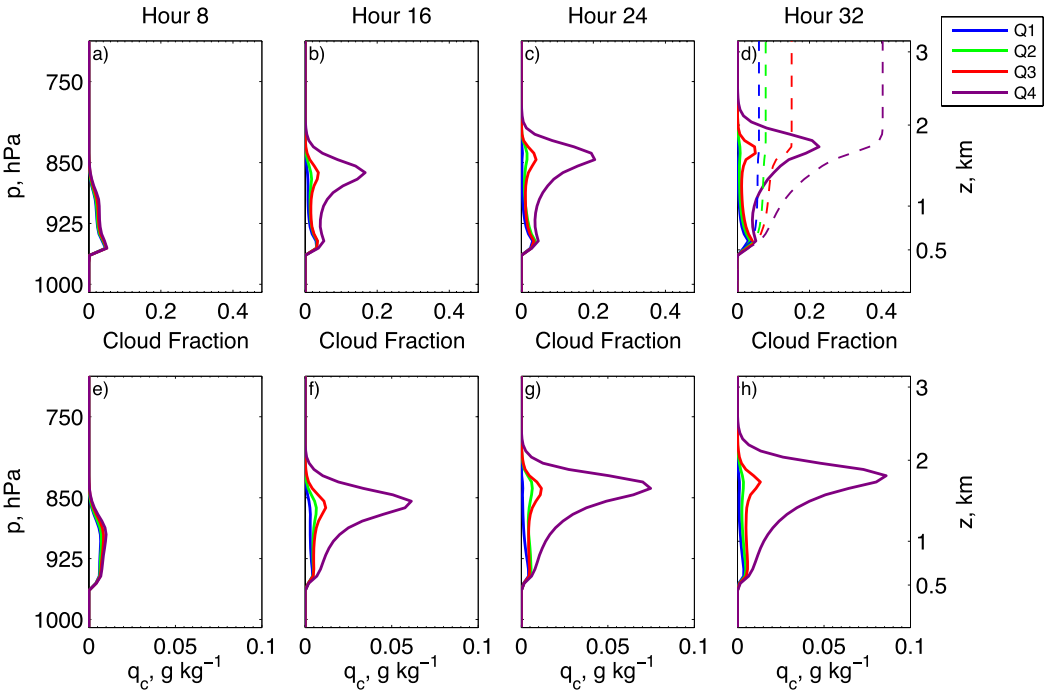

Figure 9. As in Figure 8, except for (a–d) cloud fraction and (e–h) cloud water. Quartile-sorted profiles of cumulative cloud fraction (computed upward) are plotted as dashed lines along with cloud fraction in Figure 9d.

spread out these horizontal density perturbations and inhibit them from building up on the mesoscale (Bretherton & Smolarkiewicz, 1989).

Figures 8i–8l show quartile-sorted vertical profiles of mesoscale (block-mean) perturbations of s_v/c_p, a proxy for buoyancy, averaged over 2 h periods ending at 8, 16, 24, and 32 h. As the mesoscale aggregation develops, these perturbations grow and saturate, but they remain quite small—less than 0.2 K. Thus, our simulations accurately obey the weak temperature gradient approximation (WTG) that mesoscale (block-mean) buoyancy perturbations remain negligibly small,

$$s_{vm} \approx 0, \tag{8}$$

despite significant sources of mesoscale heating and cooling due to the collective action of precipitation, radiation, turbulence, and shallow cumulus convection. Those localized heat sources instead induce mesoscale vertical motions whose associated adiabatic cooling compensates the localized heating. Like our simulations, aircraft observations of MCC are consistent with WTG. They do not show substantial mesoscale virtual temperature perturbations collocated with more humid regions and thicker clouds (Agee & Lomax, 1978).

We use a slightly modified formulation of WTG based on the observation that the mesoscale-averaged liquid water content is small at all levels in a shallow cumulus cloud field. Thus, the smallness of mesoscale-averaged variations of s_v also carries over to mesoscale-averaged variations of the virtual liquid static energy $s_{vl}=s_v-L_{vl}(q_c+q_r)$ introduced in equations (5) and (6), which is a moist-conserved variable more suitable for budget analyses. The quartile-sorted profiles of s_{vl}/c_p averaged over the 2 h period ending at 32 h are shown as dashed lines in Figure 8l. They are recognizably similar to the corresponding profiles of s_v/c_p (solid lines in the same figure) and equally small; similar results hold for other times. Hence, we can regard s_{vlm} as a reasonable mesoscale buoyancy proxy in our simulations, and our modified version of WTG is phrased:

$$s_{vlm} \approx 0. \tag{9}$$

4.3. Mesoscale Vertical Motions

Figures 8e–8h show the moisture quartile-sorted profiles of vertical motion w at the four selected times. For each altitude in each block, the mean w is the sum of the prescribed domain-mean $\overline{w}$ and the simulated

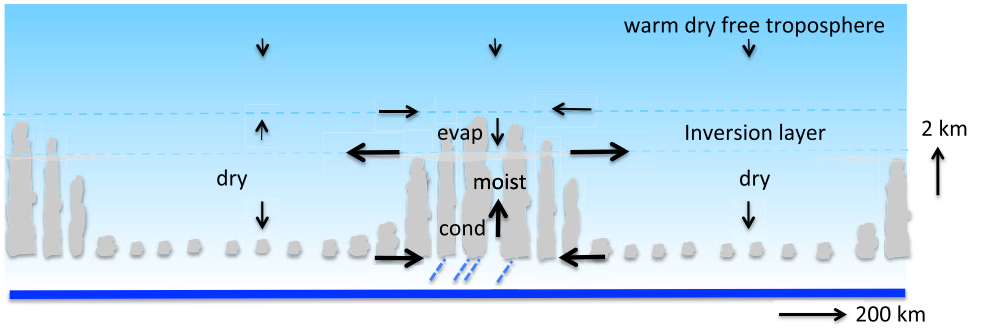

Figure 10. Schematic of processes accompanying shallow convective aggregation. On mesoscales, the virtual temperature remains flat on mesoscales but moist and dry patches develop. The moist patches support deeper and more vigorous cumulus convection, driving condensational heating and mesoscale ascent in the conditionally unstable layer and penetrative entrainment-induced evaporative cooling and mesoscale subsidence in the overlying inversion layer. The moist patches become moister via low-level humidity convergence but dry from penetrative entrainment and precipitation.

block-mean mesoscale anomaly w_m. Near the top of the cumulus layer, the latter grows to 2 cm/s averaged over the moist quartile of blocks, dominating the domain-mean subsidence. At all times, the mesoscale vertical motions have a dipole structure, with ascent in moist regions through most of the boundary layer in the moistest quartile, but descent in the inversion layer. According to WTG, these vertical motions are driven by anomalous heating of the lower part of the boundary layer and cooling of the inversion layer in moister columns, induced by small-scale turbulence and convective processes and their effects on latent, radiative and surface-driven heating. Like the profiles of liquid water, the w_m profiles quickly become asymmetric between moist and dry regions.

4.4. Conceptual Model of Aggregating Shallow Cumulus

Figure 10 presents a schematic of the aggregating boundary layer based on the results so far. This schematic will be useful for visualizing the mesoscale heat and moisture budgets, quantified in sections 5.1 and 5.2, respectively.

The blue dashed lines show the base and top of the inversion layer. They are flat because virtual temperature is approximately horizontally homogeneous (WTG). In the moist patch at the center of the diagram, cumulus updrafts lose less buoyancy to entrainment-induced evaporative cooling, so they deepen into the inversion layer and may detrain horizontally extensive patches of inversion cloud at its base. Air rising through the lower parts of these cumulus clouds condenses liquid water and releases latent heat within the mesoscale moist patch, inducing mesoscale upward motion (realized as increased updraft mass flux within the cumuli) within the moist patch. These cumuli also penetratively entrain drier air from within the inversion layer, evaporating and cooling their tops and inducing mesoscale subsidence there.

Associated with these vertical motions, there must be horizontal convergence into the moist patch throughout the lower part of the boundary layer and near the inversion top, and divergence at the inversion base. The associated net column-integrated moisture convergence helps determine whether moist patches tend to further moisten, promoting self-aggregation.

4.5. Mesoscale Cumulus Heating and Moistening

A key ingredient in our schematic is how vertical transports of heat and moisture by shallow cumulus and turbulence depend on the humidity of a mesoscale patch. Here we diagnose this dependence in the LES.

Each variable $f(\mathbf{x}, t)$ is described in terms of its domain-mean $\overline{f}$, and its deviation f' from that mean. In each block, that deviation is partitioned into the block-horizontal-mean deviation f_m and a "cumulus-scale" deviation f_c, which is the local difference of f from its block mean:

$$f(\mathbf{x}, t) = \overline{f}(t) + f'(\mathbf{x}, t), \qquad f' = f_m(\mathbf{x}, t) + f_c(\mathbf{x}, t). \tag{10}$$

With this definition, the mesoscale deviation is horizontally uniform across each block, and its horizontal average over all blocks is zero. The cumulus-scale deviation has a zero horizontal average across each block but captures the horizontal variability within that block.

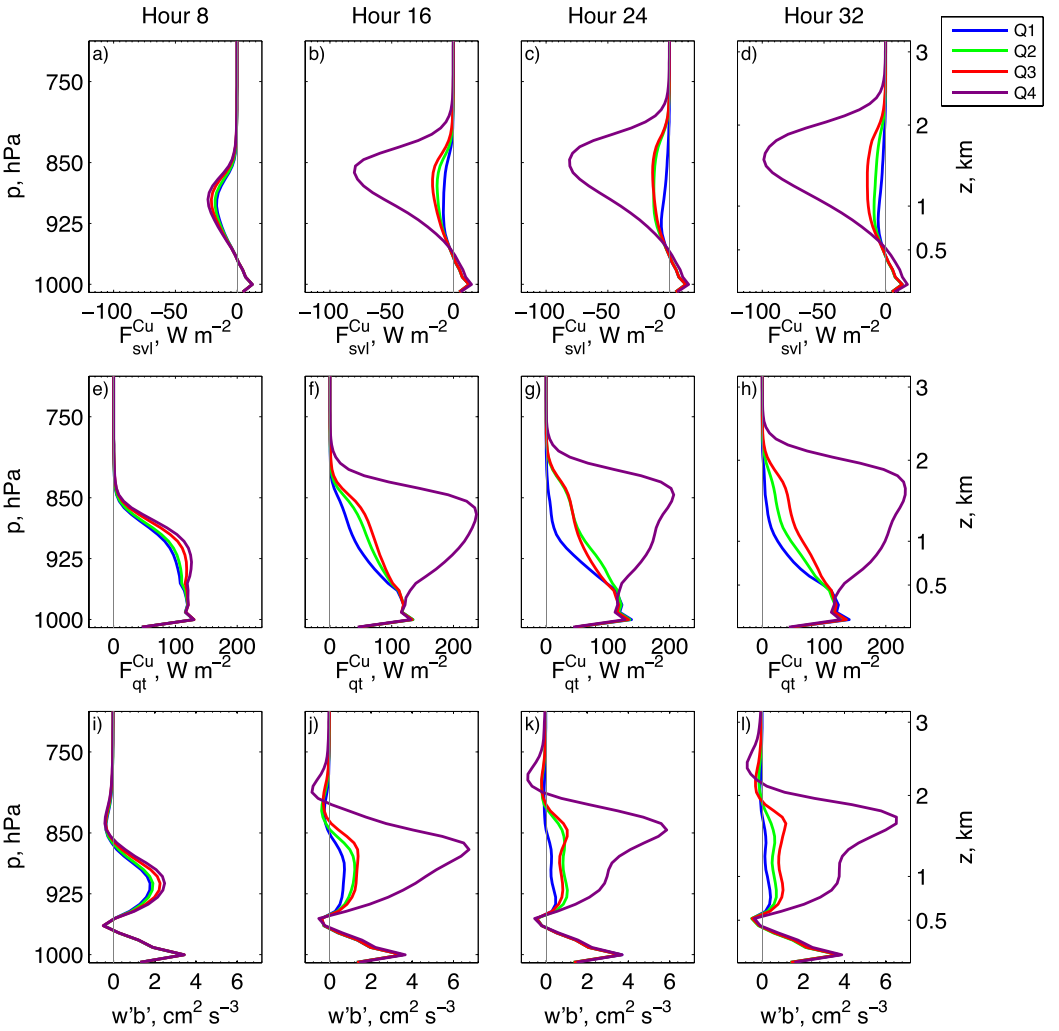

Figure 11. As in Figure 8, except for (a–d) cumulus s_{vl} flux, (e–h) cumulus q_t flux, and (i–l) buoyancy flux.

We also define the cumulus-scale covariance between two variables f and g within each block to be $[f_c g_c]$, where the square brackets indicate a horizontal average over a block. We define the block-mean vertical "cumulus" fluxes of f (which also include effects of other resolved-scale turbulence) as

$$F_f^{Cu} = \rho_0 [w_c f_c]. \tag{11}$$

Each block has a different profile of the cumulus flux of f. The domain-mean vertical flux of f is $\rho_0(\overline{w_m f_m} + \overline{[w_c f_c]})$, a sum of mesoscale and Cu-scale contributions.

Figures 11a–11h show moisture quartile-sorted profiles of the cumulus s_{vl} and q_t fluxes, which are strongest near the inversion base. The cumulus updrafts have anomalously high q_t (upward q_t flux) but low s_{vl} (downward s_{vl} flux). Below the cumulus base near 0.6 km altitude, there is no difference between the heat and moisture fluxes between the moist and dry quartiles. At hour 8, the fluxes within the cumulus layer are only slightly different between quartiles, but at later times, the fluxes are strongly concentrated in the moistest quartile, where they are also more "top-heavy," reflecting the deeper cumulus convection there. The fluxes in the moistest quartile reach maximum strength quickly, after 16 h.

According to the conceptual model, cumulus updrafts should better maintain their buoyancy as their rise in moister regions. Thus, we expect the buoyancy flux to be larger in moist regions. Figures 11i–11l show that this is indeed the case. At 16 h and later, in the moistest quartile the buoyancy flux throughout the cumulus

layer is upward throughout the cumulus layer, except in the upper reaches of the inversion, while in the other quartiles the buoyancy flux is highly suppressed more than 100 m above the cumulus base.

5. Perturbation and Mesoscale Budget Equations for Heat and Moisture

The prognostic equation for horizontal perturbations of a general prognosed scalar f with source S_f is

$$\frac{\partial f'}{\partial t} = -\mathbf{u}_h \cdot \nabla_h f' - w\frac{\partial f'}{\partial z} - w'\frac{d\bar{f}}{dz} + S_f'. \tag{12}$$

Note that unprimed quantities still include their horizontal domain mean. We will later partition this equation into mesoscale and Cu-scale components as needed.

Our LES uses the anelastic equations with a reference density profile $\rho_0(z)$. We will make use of the anelastic mass conservation equation:

$$\nabla_h \cdot \mathbf{u}_h + \rho_0^{-1}\frac{\partial}{\partial z}(\rho_0 w) = 0. \tag{13}$$

5.1. The Mesoscale s_{vl} Budget Including WTG Simplifications

For each block, we form a prognostic equation for the block averaged perturbation s_{vlm}, which we simplify using WTG. This involves block-averaging the perturbation equation (12) for s_{vl} and neglecting the tendency term on the LHS using the WTG approximation (9) that $s_{vlm} \approx 0$:

$$0 \approx \frac{\partial s_{vlm}}{\partial t} = -\left[\mathbf{u}_h \cdot \nabla_h s_{vl}' + w\frac{\partial s_{vl}'}{\partial z}\right]_m - w_m\frac{d\overline{s_{vl}}}{dz} + S_{svlm}. \tag{14}$$

WTG also implies that $s_{vl}' = s_{vlm} + s_{vlc} \approx s_{vlc}$. Using this together with the anelastic mass conservation equation (13), we can express the advection of s_{vl}' by the full velocity field as

$$\begin{aligned}
\left[\mathbf{u}_h \cdot \nabla_h s_{vl}' + w\frac{\partial s_{vl}'}{\partial z}\right]_m &= \frac{1}{\rho_0}\left[\nabla \cdot (\rho_0 \mathbf{u} s_{vl}')\right]_m \\
&= \frac{1}{\rho_0}\left[\nabla \cdot (\rho_0(\bar{\mathbf{u}} + \mathbf{u}_m + \mathbf{u}_c)s_{vlc})\right]_m \\
&= \frac{1}{\rho_0}\left[\nabla \cdot (\rho_0 \mathbf{u}_c s_{vlc})\right]_m \\
&= \left[\nabla_h \cdot (\mathbf{u}_{hc} s_{vlc})\right]_m + \frac{1}{\rho_0}\frac{\partial}{\partial z}\left[\rho_0 w_c s_{vlc}\right]_m \\
&\approx \frac{1}{\rho_0}\frac{\partial}{\partial z}\left[\rho_0 w_c s_{vlc}\right]_m.
\end{aligned} \tag{15}$$

In the final step, we justify neglecting the horizontal divergence term by applying the divergence theorem around the block, invoking scale separation between the mesoscale block size L_B and the boundary layer depth H, which we assume also scales the Cu-scale motions, and applying a scaling argument:

$$\begin{aligned}
\left[\nabla_h \cdot (\mathbf{u}_{hc} s_{vlc})\right]_m &= L_B^{-2}\int_{\partial B} (\mathbf{u}_{hc} \cdot \mathbf{n}) s_{vlc} dl \\
&\sim L_B^{-2} \cdot 4L_B \cdot U \cdot S \sim US/L_B.
\end{aligned} \tag{16}$$

Here ∂B is the horizontal block edge, U is a convective velocity scale, and S is a scale for convective s_{vl} perturbations. If we assume that w_c also scales with U, the corresponding vertical derivative term scales as

$$\frac{1}{\rho_0}\frac{\partial}{\partial z}\left[\rho_0 w_c s_{vlc}\right]_m \sim US/H. \tag{17}$$

Thus, the horizontal divergence can be neglected compared to the vertical derivative since the block size $L_B \gg H$.

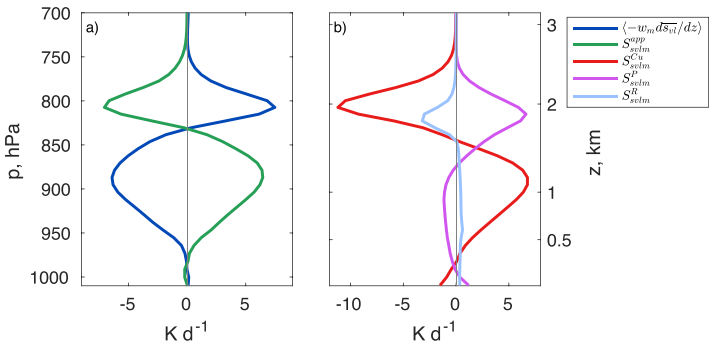

Figure 12. Profiles of moist quartile anomalies averaged over 24–32 h from the control simulation of (a) mesoscale advective warming $-w_m d\bar{s}_{vl}/dz$ and apparent heating S^{app}_{svlm}, (b) contributions to the apparent heating profile from cumulus convection, precipitation, and radiation.

Finally, the source term S_{svl} was given in the corresponding s_{vl} advection equation (7). Neglecting the very small contribution of subgrid turbulent mixing, and noting that the large-scale forcing is horizontally homogeneous, the block-mean variations of S_{svl} are due to latent heating and radiative flux convergence:

$$S_{svlm} = -\frac{1}{\rho_0}\frac{\partial}{\partial z}\left((L_v - 0.61 c_p T_0)P + F_R\right)_m. \tag{18}$$

Following Bretherton and Wyant (1997), it is convenient to define the nondimensional thermodynamic parameter:

$$\mu = 1 - 0.61 c_p T_0 / L_v \approx 0.93. \tag{19}$$

We substitute equations (15), (18), and (19) into (14):

$$0 \approx -\frac{1}{\rho_0}\frac{\partial}{\partial z}F^{Cu}_{svlm} - w_m \frac{d\bar{s}_{vl}}{dz} - \frac{1}{\rho_0}\frac{\partial}{\partial z}\left(\mu L_v P + F_R\right)_m. \tag{20}$$

This equation includes sources due to cumulus flux convergence and mesoscale vertical advection as well as the diabatic sources of s_{vl} from latent heating and radiation. In the spirit of WTG, we solve it for the block-average vertical velocity w_m in terms of the block-averaged source terms, which sum to the apparent heating S^{app}_{svlm}. In addition to the diabatic heating rates in (18) from precipitation and radiation, the apparent heating also includes a contribution from the cumulus flux convergence of s_{vl}:

$$w_m \frac{d\bar{s}_{vl}}{dz} \approx S^{app}_{svlm} = S^{Cu}_{svlm} + S^{P}_{svlm} + S^{R}_{svlm}, \tag{21}$$

where

$$\left(S^{Cu}_{svlm}, S^{P}_{svlm}, S^{R}_{svlm}\right) = -\frac{1}{\rho_0}\frac{\partial}{\partial z}\left(F^{Cu}_{svl}, \mu L_v P, F_R\right)_m. \tag{22}$$

This decomposition is analogous to similar WTG analyses for deep convection that neglected virtual effects (Chikira, 2014; Wolding & Maloney, 2015).

We test how well this applies to our control simulation averaged over a representative 8 h time interval, 24–32 h, using averages over the moistest quartile of subdomains. WTG applies more accurately for an 8 h average than for the 2 h averaging period used for earlier profile plots, because it takes time to spread mesoscale s_v anomalies across the domain. On the other hand, 8 h is still short enough to analyze the relatively slow evolution of moisture self-aggregation. Figure 12a shows that there is a close balance between the profiles of the mesoscale advective heating $-w_m d\bar{s}_{vl}/dz$ and the mesoscale apparent heating anomaly S^{app}_{svlm}, as predicted by (21) based on the WTG approximation. The vertical dipole structure of S^{app}_{svlm} shows the expected structure of apparent heating in the bulk of the cumulus layer below apparent cooling in the inversion layer.

Figure 12b shows the partitioning of the apparent heating anomaly into cumulus, precipitation and radiation contributions based on (22). The contribution from the cumulus flux is dominant, but the contribution from precipitation is also significant by this time, compensating for more than half of the cumulus-flux cooling within the inversion layer, in which the deepest cumuli reach. Between 0.1 and 1.4 km elevation (the subcloud layer and the lower part of the cumulus layer), there is slight cooling due to net evaporation of precipitation. Radiation also contributes to apparent anomalous cooling in the inversion layer, where the moist quartile has substantially more cloud.

An important difference between the three terms is their vertically integrated contribution to the apparent heating. Denote a mass-weighted column integral of any quantity f from the surface to the domain top using angle brackets:

$$\langle f \rangle = \int_0^\infty \rho_0 f \, dz. \tag{23}$$

Since the cumulus s_{vl} flux vanishes above the inversion, the column integral of its mesoscale anomaly is

$$\langle S_{svlm}^{Cu} \rangle = -\left\langle \frac{1}{\rho_0}\frac{\partial}{\partial z} F_{svl}^{Cu} \right\rangle_m = F_{svlm}^{Cu}(z=0), \tag{24}$$

which is the mesoscale anomaly of the surface s_{vl} flux. Similarly,

$$\langle S_{svlm}^{P} \rangle = \mu L_v P_m(z=0), \tag{25}$$

$$\langle S_{svlm}^{R} \rangle = -\Delta F_{Rm}, \tag{26}$$

where $P_m(z=0)$ is the surface precipitation rate anomaly, and ΔF_{Rm} is the mesoscale anomaly in the column-integrated radiative flux divergence. In the control run, there is more precipitation but also more radiative cooling in moist regions, while the surface flux anomalies are small. Thus, the column-integrated diabatic heating in Figure 12b is near zero for the cumulus fluxes, positive for the precipitation contribution, and negative for the radiatively driven contribution.

5.2. The Mesoscale Moisture Budget Equation and Humidity Self-Aggregation

In this section, we derive a mesoscale block-averaged humidity budget equation. We block-average (square brackets) the perturbation equation (12) for q_t:

$$\frac{\partial q_{tm}}{\partial t} = -\left[\mathbf{u}_h \cdot \nabla_h q_t' + w\frac{\partial q_t'}{\partial z}\right]_m - w_m \frac{d\overline{q_t}}{dz} + S_{qtm}. \tag{27}$$

Although we cannot make WTG-like simplifying approximations, we can still make the scale separation argument that

$$[\nabla_h \cdot (\mathbf{u}_{hc} q_{tc})]_m \ll \frac{1}{\rho_0}\frac{\partial}{\partial z}[\rho_0 w_c q_{tc}]_m = \frac{1}{\rho_0}\frac{\partial}{\partial z} F_{qtm}^{Cu}. \tag{28}$$

Thus,

$$\begin{aligned}
&\left[\mathbf{u}_h \cdot \nabla_h q_t' + w\frac{\partial q_t'}{\partial z}\right]_m = \left[\mathbf{u} \cdot \nabla q_t'\right]_m \\
&= \frac{1}{\rho_0}\left[\nabla \cdot (\rho_0 \mathbf{u} q_t')\right]_m \\
&= \frac{1}{\rho_0}\left[\nabla \cdot (\rho_0 (\overline{\mathbf{u}} + \mathbf{u}_m + \mathbf{u}_c)(q_{tm} + q_{tc}))\right]_m \\
&= \frac{1}{\rho_0}\left[\nabla \cdot (\rho_0 ((\overline{\mathbf{u}} + \mathbf{u}_m) q_{tm} + \mathbf{u}_c q_{tc}))\right]_m \\
&= (\overline{\mathbf{u}} + \mathbf{u}_m) \cdot \nabla q_{tm} + [\nabla_h \cdot (\mathbf{u}_{hc} q_{tc})]_m + \frac{1}{\rho_0}\frac{\partial}{\partial z}[\rho_0 w_c q_{tc}]_m \\
&\approx (\overline{\mathbf{u}} + \mathbf{u}_m) \cdot \nabla q_{tm} + \frac{1}{\rho_0}\frac{\partial}{\partial z} F_{qtm}^{Cu}.
\end{aligned} \tag{29}$$

From (3), the block-averaged humidity source term is

$$S_{qtm} = \frac{1}{\rho_0}\frac{\partial P_m}{\partial z}. \tag{30}$$

Substituting (29) and (30) into the block-averaged humidity equation (27), we obtain

$$\frac{\partial q_{tm}}{\partial t} = C_m + A_m. \tag{31}$$

The first term

$$C_m = \frac{1}{\rho_0}\frac{\partial}{\partial z}\left(P - F_{qt}^{Cu}\right)_m - w_m \frac{d\overline{q_t}}{dz}, \tag{32}$$

which Chikira (2014) named the "column process," is the combined moistening effect of the moist processes and diabatically induced vertical advection across the horizontal-mean moisture gradient. The second term

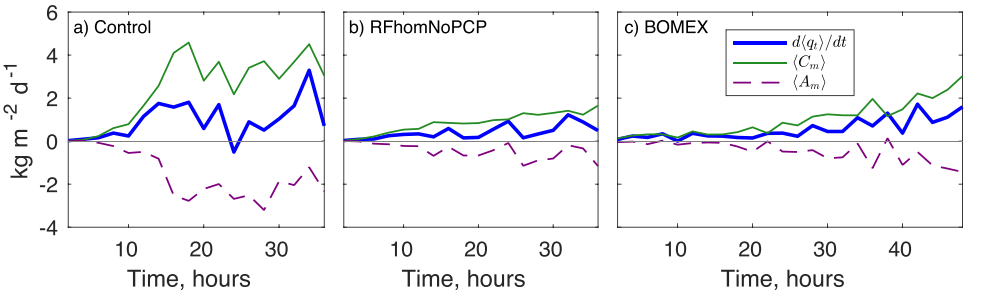

Figure 13. Time series of selected components of the moistest-quartile column-integrated moisture budget in the (a) control, (b) RFhomNoPCP, and (c) BOMEX simulations. Shown are the moistening due to the column process, advection of mesoscale perturbations and q_t storage.

$$A_m = -(\overline{\mathbf{u}} + \mathbf{u}_m) \cdot \nabla q_{tm} \tag{33}$$

is due to advection of mesoscale moisture anomalies.

Figure 13 shows time series of the column-integrated $\langle C_m \rangle$ and $\langle A_m \rangle$ averaged over the moistest quartile of blocks for the control and the two minimal-physics sensitivity simulations, along with their sum, the column moisture tendency. In all three cases, there is almost always net moisture storage in these moist blocks, amplifying their moisture anomalies. The column process generally moistens, and the moisture anomaly advection dries the columns. Early in the aggregation process (up through 12 h) $\langle C_m \rangle$ typically exceeds $\langle A_m \rangle$ by a factor of two, and for the BOMEX simulation this continues throughout the 48 h period shown. Thus, the column process is the main driver of the development of moisture self-aggregation, and $\langle C_m \rangle > 0$ appears to a necessary (though perhaps not sufficient) condition for moisture self-aggregation in this setting.

5.3. MSE Budget View of the Column Process Feedback on the Humidity Budget

A useful way to analyze the column process moistening tendency is to rephrase it in terms of moist static energy (MSE) $h = c_p T + L_v q_v + gz = s_l + L_v q_t$, which has the advantage of not being directly affected by liquid precipitation. From (5),

$$h = s_{vl} + \mu L_v q_t. \tag{34}$$

Applying the WTG approximation $s_{vlm} \approx 0$, this equation implies that mesoscale MSE anomalies are proportional to the humidity anomalies:

$$h_m \approx \mu L_v q_{tm}. \tag{35}$$

Similarly, adding the s_{vl} equation (20) to μL_v times equation (32) defining the column process,

$$\mu L_v C_m = -w_m \frac{d\overline{h}}{dz} - \frac{1}{\rho_0}\frac{\partial}{\partial z}\left(F_R + F_h^{Cu}\right)_m, \tag{36}$$

$$\mu L_v \langle C_m \rangle = -\left\langle w_m \frac{\partial \overline{h}}{\partial z} \right\rangle + F_{hm}^{Cu}(z=0) - \Delta F_{Rm}. \tag{37}$$

This decomposition of $\langle C_m \rangle$ naturally arises from constructing a block-average column MSE budget, as used in the study of deep-convective self-aggregation (Bretherton et al., 2005).

Figure 14 shows time series of the terms of (37) averaged over the moistest quartile of blocks in the control run. The vertical advection term is positive and dominates the surface flux and radiation terms. In the vocabulary of deep-convective organization (Raymond et al., 2009), this is called negative gross moist stability (Yu et al., 1998), i.e., mesoscale circulations acting on the horizontal-mean thermodynamic profiles converge MSE into columns with already high MSE.

The sign of this vertical advection term for shallow convection is driven by the decrease of domain-mean MSE $\overline{h}(z)$ with height, coupled to the structure of the mesoscale vertical motions driven by the apparent heating. Anomalous mesoscale ascent in the cumulus layer of the moist regions drives a positive contribution to $\langle C_m \rangle$, while the descent in the inversion layer drives a negative contribution. Even without

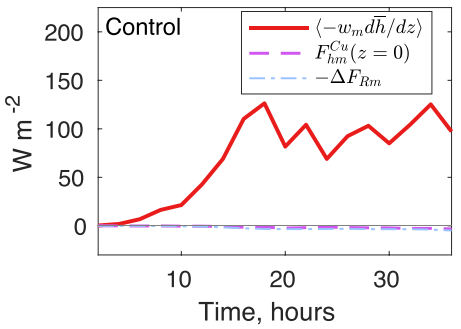

Figure 14. Time series of the contributions to moist-quartile column moistening $\langle C_m \rangle$ from vertical MSE advection, anomalous surface fluxes, and anomalous column radiative heating.

precipitation, the positive contribution outweighs the negative, as argued in section 6. As precipitation increases within moist columns, the associated net latent heating enhances the upward motions in the cumulus layer and diminishes the evaporatively driven downward motions in the inversion layer, further increasing the gross moist instability.

Figure 14 also shows that the anomalous column radiative heating $-\Delta F_{Rm}$ is slightly negative in anomalously moist columns, apparently acting to counter self-aggregation. The extra cloud and water vapor in the moist columns enhance boundary layer radiative cooling. The anomalous surface flux $F_{hm}^{Cu}(z{=}0)$ is also small and slightly negative in moist columns. Both of these results are opposite to the initial stages of deep-convective self-aggregation, in which extensive anvil cirrus clouds and vigorous cold pools decrease radiative cooling and increase surface fluxes in moist columns (Bretherton et al., 2005). From the column MSE budget perspective, shallow convective self-aggregation is fundamentally driven by mesoscale advective feedbacks, while deep-convective self-aggregation is driven by radiative and surface flux feedbacks.

Following Chikira (2014), one could also process-partition the column process moistening tendency by separating the contribution to mesoscale vertical motions from heating by different physical processes (e.g., cumulus fluxes, precipitation, and radiation) that can be added to the direct moistening contribution from those processes. Although this approach is attractive in principle, and useful in special cases (see section 6) it did not lead us to additional general insights about our simulations because the cumulus fluxes, radiative heating and precipitation are highly interdependent. For instance, the RFhom sensitivity study suggests that allowing horizontally inhomogeneous radiative heating speeds up self-aggregation. However, the anomalous radiative heating leads to a negative contribution $-\Delta F_{Rm}$ to the anomalous column MSE tendency in moist columns. That extra radiative cooling also induces mesoscale downward motion, producing an additional advective MSE sink (not shown). Thus, according to the budget approach, both the direct and circulation-induced radiative contributions appear to disfavor self-aggregation. This apparent contradiction can be resolved by recognizing that anomalous radiative cooling in the inversion layer destabilizes the underlying boundary layer and stimulates more cumulus convection in moist columns, which acts as a MSE source. This illustrates the limitations of budget approaches to predicting how a complex interconnected system will respond to changed conditions.

5.4. What Limits the Amplitude of Self-Aggregation?

In our simulations, self-aggregation of TWP tends to slow down once the quartile TWP anomalies reach 5–10% of the domain-mean TWP. Our budget analysis suggests that as humidity aggregation intensifies, these moisture anomalies increasingly get advected out of the moist regions, as encapsulated in the term $\langle A_m \rangle$ in the moisture budget (31). Using (33), this term can be broken down:

$$\langle A_m \rangle = -\langle \overline{\mathbf{u}}_h \cdot \nabla_h q_{tm} \rangle - \langle \overline{w} \partial q_{tm}/\partial z \rangle - \langle \overline{\mathbf{u}}_m \cdot \nabla q_{tm} \rangle. \quad (38)$$

We ran our LES in a reference frame moving with approximately the mean boundary layer wind, as noted in section 2.3. This is advantageous for moisture budget analysis, because otherwise the boundary layer-mean wind would rapidly advect mesoscale anomalies between subdomains.

In such a reference frame, the three terms all tend to damp mesoscale humidity anomalies. The first term, the horizontal advection of q_{tm} by a vertically varying mean wind, can shear out moisture anomalies. The second term, due to mean subsidence, damps mesoscale humidity perturbations by squashing them toward the surface on a divergence time scale. The third term, advection by mesoscale circulations, horizontally mixes the anomalously moist and dry regions. It becomes increasingly effective as the moisture anomalies and mesoscale circulations strengthen.

6. Mesoscale Humidity Aggregation in the Minimal-Physics Case

We now consider what the mesoscale column moisture budget, together with WTG, implies about the development of mesoscale humidity aggregation in the minimal-physics case of no-precipitation and no

mesoscale variation of radiation or surface fluxes, since our sensitivity tests shows that these restrictions do not prevent aggregation in the S6 and BOMEX cases.

6.1. Importance of a Concave $\overline{h}-\overline{s}_{vl}$ Curve

In the minimal-physics case, the source terms in the budgets for mesoscale anomalies of s_{vl}, q_t, and h due to mesoscale anomalies of precipitation, radiation and surface fluxes all vanish. The column moistening due to the column process is entirely due to mesoscale advection across the mean vertical gradients induced by apparent heating from the cumulus fluxes:

$$\langle C_m \rangle = -\langle w_m d\overline{h}/dz \rangle. \tag{39}$$

In the minimal-physics case, the mesoscale anomaly in the apparent heating profile, defined in equation (21), is due only to the convergence of the anomalous cumulus s_{vl} flux. This is positive in the cumulus layer due to updraft condensational heating, and negative in the inversion layer due to evaporative cooling. However, since we assume no mesoscale anomalies of the s_{vl} flux in the minimal-physics case, the anomalous s_{vl} flux has a zero vertical integral. The vertical integral of equation (21) then implies that

$$0 = \langle w_m d\overline{s}_{vl}/dz \rangle. \tag{40}$$

Comparing equations (39) and (40), were there a "mixing line" relationship between $\overline{h}(z)$ and $\overline{s}_{vl}(z)$, or equivalently, between $\overline{q}_t(z)$ and $\overline{s}_{vl}(z)$, their vertical gradients would be linearly proportional and the column moistening due to the cumulus convection would be zero.

However, Figures 15a and 15b show that for the thermodynamic profiles that we have been simulating in our two minimal-physics cases, $\overline{h}(z)$ is a generally concave function of $\overline{s}_{vl}(z)$. Following Chikira (2014), we define a nondimensional measure of the vertical MSE gradient to the dry stratification:

$$\alpha_h(z,t) = -\frac{d\overline{h}/dz}{d\overline{s}_{vl}/dz}. \tag{41}$$

This is the negative slope of the $\overline{h}(z)$-$\overline{s}_{vl}(z)$ curve, which can easily be visualized from Figures 15a and 15b. A concave $\overline{h}(z)$-$\overline{s}_{vl}(z)$ curve is equivalent to α_h decreasing with $\overline{s}_{vl}(z)$ and thus with height. In both minimal-physics cases, α_h decreases from nearly infinity in the subcloud layer to near zero near the inversion top.

Figure 15c shows the vertical profiles of $-w_m d\overline{h}/dz$ and $w_m d\overline{s}_{vl}/dz$ for RFhomNoPCP at 32 h. At each height, their ratio is $\alpha_h(z)$. Consistent with the $\overline{h}(z)$-$\overline{s}_{vl}(z)$ curve, $-w_m d\overline{h}/dz$ is much larger than $w_m d\overline{s}_{vl}/dz$ in the subcloud and lower cumulus layer. Above this level, they are comparable, except near the inversion top, where $-w_m d\overline{h}/dz$ becomes smaller than $w_m d\overline{s}_{vl}/dz$. On the right of Figure 15c are layer-mean values of $\alpha_h(z,t)$ calculated as ratios of the layer integrals of the plotted curves for the subcloud, subinversion

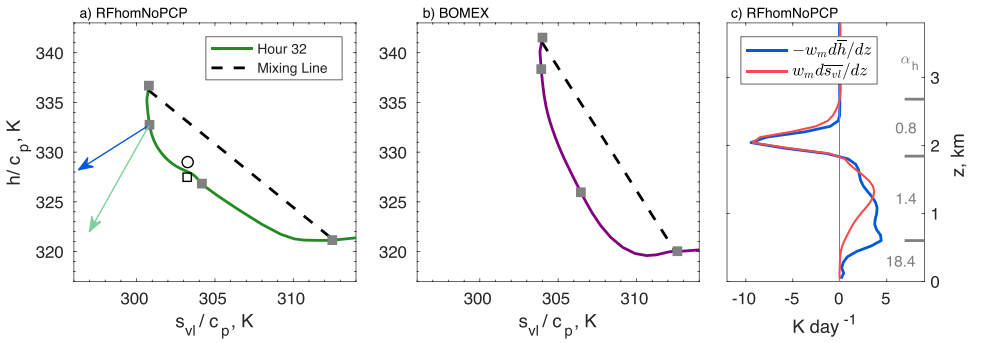

Figure 15. Plot of $\overline{h}(z)$ versus $\overline{s}_{vl}(z)$ at 32 h, in the (a) RFhomNoPCP and (b) BOMEX simulations. The grey squares indicate the surface, cumulus base, inversion base and inversion top. For RFhomNoPCP, these correspond to $z \approx 0$, 0.6, 1.8, and 2.7 km. A black dashed mixing line is shown between the surface grid level and the inversion top. In Figure 15a, the arrows indicate how radiative cooling (blue) and cold advection (light green) pull the $\overline{h}$-$\overline{s}_{vl}$ curve away from the mixing line, while the black circle and square in Figure 15a show the moist (Q4) and dry (Q1) quartile means at 1.5 km altitude. (c) Shows the moist-quartile profiles of the mesoscale vertical advective cooling (red) and MSE source (blue) for RFhomNoPCP, and average values of the Chikira parameter α_h for the subcloud, cumulus, and inversion layers.

cumulus and inversion layers. The subcloud-mean α_h exceeds 18. Averaged between the cumulus cloud base and the inversion, α_h is 1.4, while in the inversion layer α_h is only 0.8.

Comparing these profiles, the general decrease of α_h with height is exactly what is needed to make the vertical integral $\langle w_m d\overline{h}/dz \rangle$ positive, even though the vertical integral $\langle w_m d\bar{s}_{vl}/dz \rangle$ is zero. Indeed, following Chikira (2014), the mesoscale advective feedback term can written as a weighted average of the apparent heating rate using WTG, as expressed in (21):

$$-\left\langle w_m \frac{\partial \overline{h}}{\partial z} \right\rangle = \langle \alpha_h S_{svlm}^{app} \rangle. \tag{42}$$

For the minimal-physics case, there is a positive lobe of S_{svlm}^{app} low in the boundary layer, where α_h is large, and a negative lobe of equal vertical integral in the inversion layer, where α_h is small. This ensures that the weighted average $\langle \alpha_h S_{svlm}^{app} \rangle > 0$, i.e., negative gross moist stability and positive moisture convergence into moist columns from the mesoscale advection contribution to the column process.

The inclusion of shallow cumulus precipitation would amplify the positive lobe and diminish the negative lobe of $\langle S_{svlm}^{app} \rangle$. As long as $\overline{h}$ is a decreasing function of height (so $\alpha_h > 0$) through the shallow cumulus layer, this will help make $\langle \alpha_h S_{svlm}^{app} \rangle$ positive and strengthen the convergence feedback on amplifying mesoscale moisture anomalies.

6.2. Origin of a Concave $\overline{h} - \bar{s}_{vl}$ Curve

Pure turbulent and convective mixing would establish vertical profiles of $\overline{h}(z)$ versus $\bar{s}_{vl}(z)$ that would trace out a mixing line on the $\overline{h}(z) - \bar{s}_{vl}(z)$ plot, with end points corresponding to air from the subcloud layer and the free troposphere just above the inversion top. In Figures 15a and 15b, this mixing line is indicated by black dashes.

A concave $\overline{h}(z)$-$\bar{s}_{vl}(z)$ curve and the associated decrease of $\alpha_h(z)$ with height can be maintained in typical cloud-topped boundary layers by a combination of radiative cooling and cold advection. Mean boundary layer radiative cooling reduces the s_{vl} of boundary layer air without affecting its q_t, pulling the $\overline{h}(z)$-$\bar{s}_{vl}(z)$ curve leftward and downward between the end points of the mixing line to create a concave shape, as shown by the blue arrow in Figure 15a. Horizontal advection of cold, dry air reduces both the s_{vl} and q_t of boundary layer air, pulling the curve to the left and even more strongly downward (light green arrow in Figure 15a) to add to its concavity. The effect of these processes in creating deviations from a mixing line is larger in a shallow cumulus boundary layer, where the turnover time scale in the cumulus layer and especially the inversion layer is many hours, than in a well-mixed stratocumulus-capped boundary layer with a much shorter eddy turnover time (Bretherton et al., 1995).

It is interesting to consider how the horizontal mesoscale temperature-humidity variability in the schematic of Figure 10 fits into this description. At a given altitude, e.g., the inversion base, s_{vl} is constant while q_t and hence h varies between the dry and moist regions. This structure would trace out a vertical line in the h-s_{vl} plot. The open square and circle in Figure 15a shows the points on this plot corresponding to the dry (Q1) and moist (Q4) quartiles at 1.5 km altitude at 32 h. As expected, the moist-quartile point lies above the dry-quartile plot and is thus closer to the mixing line, reflecting the more vigorous vertical mixing in the active cumulus convection of the moist regions.

A peculiarity visible in Figure 15a is a slight reversal in the $\overline{h}(z)$-$\bar{s}_{vl}(z)$ concavity arising from elevations between 1.5 and 2 km. This is a layer that is actually above the inversion base in the ECMWF summertime climatological profile from which this case was derived. Because the inversion in this region slopes down toward the east (the upwind direction), there is horizontal advective warming and drying at this level, rather than the cooling and moistening characteristic of the interior of the boundary layer. This advective forcing pulls the $\overline{h}(z)$-$\bar{s}_{vl}(z)$ slightly up and right in that layer. Because the simulated boundary layer is somewhat deeper than that in the ECMWF climatology, that feature is artificially moved down into its interior.

6.3. Relation to the Theory of Entrainment-Related Mesoscale Production of Humidity Variance

In section 1, we suggested that our analysis is related to the theory of entrainment-induced mesoscale production of humidity variance outlined by Jonker et al. (1999) and De Roode et al. (2004). One connection is formal. The question of whether moist blocks get moister is similar to asking whether the domain-mean

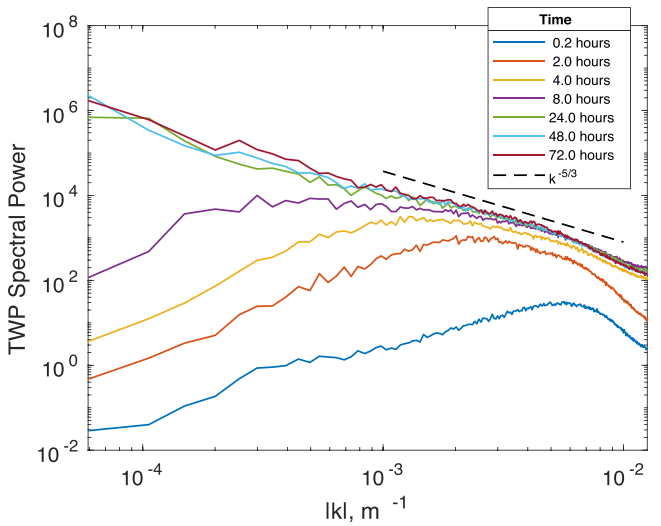

Figure 16. Spectrum of total water path versus magnitude $|k|$ of horizontal two-dimensional wave number at a sequence of times in the control simulation.

mesoscale humidity variance increases. Formally, one could multiply our equation (27) for the tendency dq_{tm}/dt by $2q_{tm}$ and horizontally average across all the blocks to get an equation for the tendency of the mesoscale humidity variance $\overline{q_{tm}^2}$. As discussed above, a critical term on the right hand of (27) is $-w_m d\overline{q}_t/dz$; its contribution to the mesoscale humidity variance tendency is $-2q_m w_m d\overline{q}_t/dz$, consistent with the variance budget equation in De Roode et al. (2004).

A second related connection is the finding of Jonker et al. (1999) that in a dry-convective boundary layer, only scalars that are not linearly related to the virtual potential temperature undergo mesoscale variance growth. De Roode et al. (2004) found analogous results for stratocumulus-like mixed layers. For our minimal-physics case, we found that in a shallow cumulus boundary layer, growth of column q_{tm} variance will not occur if $\overline{q}_t$ is a linear function of $\overline{s}_{vl}$, which is our analogue to virtual potential temperature. Although the vertical structures of $\overline{q}_t$ and $\overline{s}_{vl}$ are vastly different between a dry-convective or stratocumulus-capped mixed layer, these results both can be traced to the conditions needed to obtain positive mesoscale variance production of humidity in a fluid which cannot support large horizontal variations in density.

Fourier spectra of total water path from our control simulation (Figure 16) show a long-wavelength tail analogous to similar spectra from LES of closed-cell convection, e.g., Figure 4 of Schroeter et al. (2005), with steady growth of power at low wave numbers that saturates into a behavior not far from an $O(|k|^{-5/3})$ power law; the saturation takes longer for lower wave numbers and is complete after 24 h, with little further spectral change out to 72 h. A qualitatively similar evolution is even seen in the Fourier spectrum of a passive scalar in a dry-convective boundary layer (Jonker et al., 1999). However, in a moist boundary layer, unlike a dry-convective boundary layer, humidity is not a passive scalar but leads to clouds which can cause latent and radiative heating that feed back on the mesoscale circulations, which in turn help amplify the mesoscale humidity variance.

7. Discussion and Conclusions

Large-domain $(128\ \text{km})^2$ large-eddy simulations of northeastern Pacific shallow cumulus convection spontaneously and robustly develop mesoscale humidity and cloud aggregation within 1–3 days, even if precipitation or mesoscale radiative and surface flux feedbacks are suppressed.

We used the weak temperature gradient approximation to develop a conceptual model of shallow cumulus self-aggregation as an instability of a horizontally homogeneous field of cumulus clouds in which humidity-convection feedbacks spontaneously amplify mesoscale moist and dry patches. This framing is similar to theories of deep-convective self-aggregation. However, the aggregation mechanisms are different for shallow versus deep convection because of their different vertical structures of the mesoscale vertical velocity and moist static energy profiles. Deep convection requires mesoscale radiative feedback to aggregate. The associated vertical circulations have positive gross moist stability, i.e., in the net they diverge MSE out of moist, high MSE, columns, opposing and slowing the aggregation process. Shallow convection aggregates quickly through a purely dynamical mechanism because it has negative gross moist stability; the mesoscale vertical motions and MSE profile are configured so as to converge MSE into moist columns. We argued that in the simplest case of nonprecipitating cumulus clouds, this negative gross moist stability is due to the mean radiative cooling of the boundary layer.

As the cumuli in moist regions precipitate more, driving mesoscale ascent with their latent heating, the overlying evaporatively driven subsidence becomes less important. With a typical tropical MSE profile, we speculate that this mesoscale vertical motion profile will keep gross moist stability negative (promoting continued aggregation) until the cumulus layer deepens enough to glaciate, after which a deep-convective view of self-aggregation must be adopted.

In section 6.3, we noted connections of our analysis methods and results with earlier work on mesoscale production of humidity variance related to entrainment of free-tropospheric air into dry-convective and stratocumulus-capped mixed layers, inspired in part by observations and LES of closed MCC. Further comparing the feedback mechanisms supporting the self-aggregation of humidity and cloud in different types of cloud-topped boundary layers is a worthy topic of future research.

Our results differ from the finding of Seifert and Heus (2013) that precipitation, and in particular, the subcloud evaporation of precipitation, is essential to mesoscale self-aggregation in the "moist RICO" case they simulated. There are differences of model configuration—the domain size for their sensitivity experiments was only 20% as large in each horizontal dimension as ours, and might not support the same kind of moisture aggregation. Their horizontal and vertical grid are also much finer; in simulations of deep-convective radiative-convective equilibrium, this is found to inhibit the initial development of self-aggregation (Muller & Held, 2012). Their microphysical parameterization is different. As in our BOMEX case, the aggregation in their nonprecipitating sensitivity simulation might be too slow to be obvious in the cloud field after 30 h, even though it would be clear in a simulation twice as long. Lastly, and again in contrast to Seifert and Heus (2013), it is intriguing that numerical simulations of radiative-convective equilibrium suggest that self-aggregation occurs in smaller domains (Jeevanjee & Romps, 2013) and without the help of mesoscale radiative feedbacks (Muller & Bony, 2015) if the evaporation of precipitation is suppressed. The aggregation mechanism in these simulations is strongly connected to the development of shallow mesoscale circulations and may be qualitatively similar to the one we find in our simulations. More study of these sensitivities to model, resolution, and cloud regime is warranted.

One foundation of the conceptual model is that the shallow cumulus clusters favor mesoscale regions of higher water vapor path. A more extensive statistical analysis of this correlation in satellite observations would be useful. Another aspect of this model amenable to observational testing is the dipole profile of vertical velocity within the convectively active patches.

Acknowledgments
We acknowledge support from Department of Energy ASR grant DE-SC0011602 and National Science Foundation grant AGS-1445813, and Marat Khairoutdinov for developing and managing the System for Atmospheric Modeling. Rob Wood and two anonymous referees provided constructive advice. The SAM block budget diagnostics were based on an earlier implementation by Matt Peters. The model output and Matlab scripts used to generate the analyses and figures in this paper are stored in the University of Washington ResearchWorks Archive and can be obtained at http://hdl.handle.net/1773/39708.

References

Agee, E. M., Chen, T. S., & Dowell, K. E. (1973). A review of mesoscale cellular convection. *Bulletin of the American Meteorological Society*, *54*, 1004–1012.

Agee, E. M., & Lomax, F. E. (1978). Structure of the mixed layer and inversion layer associated with patterns of mesoscale cellular convection during AMTEX 1975. *Journal of the Atmospheric Sciences*, *35*, 2281–2301.

Berner, A. H., Bretherton, C. S., Wood, R., & Muhlbauer, A. (2013). Marine boundary layer cloud regimes and POC formation in an LES coupled to a bulk aerosol scheme. *Atmospheric Chemistry and Physics*, *13*, 12549–12572. https://doi.org/10.5194/acp-13-12549-2013

Blossey, P. N., Bretherton, C. S., & Wyant, M. C. (2009). Subtropical low cloud response to a warmer climate in a superparameterized climate model. Part II: Column modeling with a cloud resolving model. *Journal of Advances in Modeling Earth Systems*, *1*, 8. https://doi.org/10.3894/JAMES.2009.1.8

Blossey, P. N., Bretherton, C. S., Zhang, M., Cheng, A., Endo, S., Heus, T., . . . Xu, K.-M. (2013). Marine low cloud sensitivity to an idealized climate change: The CGILS LES intercomparison. *Journal of Advances in Modeling Earth Systems*, *5*, 234–258. https://doi.org/10.1002/jame.20025

Bretherton, C. S., Austin, P., & Siems, S. T. (1995). Cloudiness and marine boundary layer dynamics in the ASTEX Lagrangian experiments. Part II: Cloudiness, drizzle, surface fluxes and entrainment. *Journal of the Atmospheric Sciences*, *52*, 2724–2735.

Bretherton, C. S., Blossey, P. N., & Khairoutdinov, M. (2005). An energy-balance analysis of deep convective self-aggregation above uniform SST. *Journal of the Atmospheric Sciences*, *62*, 4273–4292.

Bretherton, C. S., & Smolarkiewicz, P. K. (1989). Gravity waves, compensating subsidence and detrainment around cumulus clouds. *Journal of the Atmospheric Sciences*, *46*, 740–759.

Bretherton, C. S., & Wyant, M. C. (1997). Moisture transport, lower tropospheric stability and decoupling of cloud-topped boundary layers. *Journal of the Atmospheric Sciences*, *54*, 148–167.

Chikira, M. (2014). Eastward-propagating intraseasonal oscillation represented by Chikira-Sugiyama cumulus parameterization. Part II: Understanding moisture variation under weak temperature gradient balance. *Journal of the Atmospheric Sciences*, *71*, 615–639. https://doi.org/10.1175/JAS-D-13-038.1

De Roode, S. R., Duynkerke, P. G., & Jonker, H. M. M. (2004). Large-eddy simulation: How large is large enough? *Journal of the Atmospheric Sciences*, *64*, 403–421.

Emanuel, K., Wing, A. A., & Vincent, E. M. (2014). Radiative-convective instability. *Journal of Advances in Modeling Earth Systems*, *6*, 75–90. https://doi.org/10.1002/2013MS000270

Fiedler, B. H. (1984). The mesoscale stability of entrainment into cloud-topped mixed layers. *Journal of the Atmospheric Sciences*, *41*, 92–101.

Geoffroy, O., Brenguier, J.-L., & Burnet, F. (2010). Parametric representation of the cloud droplet spectra for LES warm bulk microphysical schemes. *Atmospheric Chemistry and Physics*, *10*, 4835–4848. https://doi.org/10.5194/acp-10-4835-2010

Held, I. M., Hemler, R. S., & Ramaswamy, V. (1993). Radiative-convective equilibrium with explicit two-dimensional convection. *Journal of the Atmospheric Sciences*, *50*, 3909–3927.

Jeevanjee, N., & Romps, D. M. (2013). Convective self-aggregation, cold pools, and domain size. *Geophysical Research Letters*, *40*, 994–998. https://doi.org/10.1002/grl.50204

Johnson, R. H., & Nicholls, M. E. (1983). A composite analysis of the boundary layer accompanying a tropical squall line. *Monthly Weather Review*, *111*, 308–319.

Jonker, H. J. J., Duynkerke, P. G., & Cuijpers, J. W. M. (1999). Mesoscale fluctuations in scalars generated by boundary layer convection. *Journal of the Atmospheric Sciences*, *56*, 801–808.

Kazil, J., Yamaguchi, T., & Feingold, G. (2017). Mesoscale organization, entrainment, and the properties of a closed-cell stratocumulus cloud. *Journal of Advances in Modeling Earth Systems*, *9*, 2214–2229. https://doi.org/10.1002/2017MS001072

Khairoutdinov, M. F., & Kogan, Y. L. (2000). A new cloud physics parameterization in a large-eddy simulation model of marine stratocumulus. *Monthly Weather Review*, *128*, 229–243.

Khairoutdinov, M. F., & Randall, D. A. (2003). Cloud resolving modeling of the ARM Summer 1997 IOP: Model formulation, results, uncertainties, and sensitivities. *Journal of the Atmospheric Sciences*, *60*, 607–625.

LeMone, M. A., & Meitin, R. J. (1984). Three examples of fair-weather mesoscale boundary layer convection in the tropics. *Monthly Weather Review*, *112*, 1985–1997.

Malkus, J. S., & Riehl, H. (1964). *Cloud structure and distribution over the tropical Pacific Ocean* (229 pp.). Berkley: University of California Press.

Mlawer, E. J., Taubman, S. J., Brown, P. D., Iacono, M. J., & Clough, S. A. (1997). RRTM, a validated correlated-k model for the longwave. *Journal of Geophysical Research*, *102*, 663–682. https://doi.org/10.1029/97JD00237

Morrison, H., Curry, J. A., & Khvorostyanov, V. I. (2005). A new double-moment microphysics parameterization for application in cloud and climate models. Part I: Description. *Journal of the Atmospheric Sciences*, *62*, 1665–1677. https://doi.org/10.1175/JAS3446.1

Mueller, G., & Chlond, A. (1996). Three-dimensional numerical study of cell broadening during cold air outbreaks. *Boundary-Layer Meteorology*, *81*, 289–323.

Muller, C., & Bony, S. (2015). What favors convective aggregation and why? *Geophysical Research Letters*, *42*, 5626–5634. https://doi.org/10.1002/2015GL064260

Muller, C. J., & Held, I. M. (2012). Detailed investigation of the self-aggregation of convection in cloud resolving simulations. *Journal of the Atmospheric Sciences*, *69*, 2551–2565. https://doi.org/10.1175/JAS-D-11-0257.1

Neale, R. B., Chen, C.-C., Gettelman, A., Lauritzen, P. H., Park, S., Williamson, D. L., . . . Taylor, M. A. (2012). *Description of the NCAR Community Atmosphere Model (CAM 5.0)* (NCAR Tech. Note NCAR/TN-486+STR, 273 pp.). Boulder, CO: National Center for Atmospheric Research.

Nuijens, L., Serikov, I., Hirsch, L., Lonitz, K., & Stevens, B. (2014). The distribution and variability of low-level cloud in the North Atlantic trades. *Quarterly Journal of the Royal Meteorological Society*, *140*, 2364–2374. https://doi.org/10.1002/qj.2307

Raymond, D. J., Sessions, S. L., Sobel, A. H., & Fuchs, Ž. (2009). The mechanics of gross moist stability. *Journal of Advances in Modeling Earth Systems*, *1*, 9. https://doi.org/10.3894/JAMES.2009.1.9

Rothermel, J., & Agee, E. M. (1980). Aircraft investigation of mesoscale cellular convection during AMTEX 1975. *Journal of the Atmospheric Sciences*, *37*, 1027–1040.

Schroeter, M., Raasch, S., & Jansen, H. (2005). Cell broadening revisited: Results from high-resolution large-eddy simulations of cold air outbreaks. *Journal of the Atmospheric Sciences*, *62*, 2023–2032. https://doi.org/10.1175/JAS3451.1

Seifert, A., & Heus, T. (2013). Large-eddy simulation of organized precipitating trade wind cumulus clouds. *Atmospheric Chemistry and Physics*, *13*, 5631–5645. https://doi.org/10.5194/acp-13-5631-2013

Seifert, A., Heus, T., Pincus, R., & Stevens, B. (2015). Large-eddy simulation of the transient and near-equilibrium behavior of precipitating shallow convection. *Journal of Advances in Modeling Earth Systems*, *7*, 1918–1937. https://doi.org/10.1002/2015MS000489

Siebesma, A. P., Bretherton, C. S., Brown, A., Chlond, A., Cuxart, J., Duynkerke, P. G., . . . Stevens, D. E. (2003). A large eddy simulation intercomparison study of shallow cumulus convection. *Journal of the Atmospheric Sciences*, *60*, 1201–1219.

Sobel, A., & Bretherton, C. (2000). Modeling tropical precipitation in a single column. *Journal of Climate*, *13*, 4378–4392.

Tobin, I., Bony, S., & Roca, R. (2012). Observational evidence for relationships between the degree of aggregation of deep convection, water vapor, surface fluxes, and radiation. *Journal of Climate*, *25*, 6885–6904.

Tompkins, A. M. (2001). Organization of tropical convection in low vertical wind shears: The role of water vapor. *Journal of the Atmospheric Sciences*, *58*, 529–545.

Vogel, R., Nuijens, L., & Stevens, B. (2016). The role of precipitation and spatial organization in the response of trade-wind clouds to warming. *Journal of Advances in Modeling Earth Systems*, *8*, 843–862. https://doi.org/10.1002/2015MS000568

Wang, H., & Feingold, G. (2009). Modeling mesoscale cellular structures and drizzle in marine stratocumulus. Part II: The microphysics and dynamics of the boundary regions between open and closed cells. *Journal of the Atmospheric Sciences*, *66*, 3257–3275.

Wolding, B. O., & Maloney, E. D. (2015). Objective diagnostics and the Madden-Julian Oscillation. Part II: Application to moist static energy and moisture budgets. *Journal of Climate*, *28*, 7786–7808. https://doi.org/10.1175/JCLI-D-14-00689.1

Wood, R., & Hartmann, D. L. (2006). Spatial variability of liquid water path in marine low cloud: The importance of mesoscale cellular convection. *Journal of Climate*, *19*, 1748–1764.

Xue, H., Feingold, G., & Stevens, B. (2008). The role of precipitating cells in organizing shallow convection. *Journal of the Atmospheric Sciences*, *65*, 392–406.

Yu, J.-Y., Chou, C., & Neelin, J. D. (1998). Estimating the gross moist stability of the tropical atmosphere. *Journal of the Atmospheric Sciences*, *55*, 1354–1372. https://doi.org/10.1175/1520-0469(1998)055<1354:ETGMSO>2.0.CO;2